

MICROSTRUCTURAL STABILITY AND HYDROGEN SOLUBILITY

IN $a - Si_{1-x}Ge_x:H$

ARTHUR LAKES LIBRARY
COLORADO SCHOOL OF MINES
GOLDEN, CO 80401

by

Nam Hyun Kang

ProQuest Number: 10794289

All rights reserved

INFORMATION TO ALL USERS

The quality of this reproduction is dependent upon the quality of the copy submitted.

In the unlikely event that the author did not send a complete manuscript and there are missing pages, these will be noted. Also, if material had to be removed, a note will indicate the deletion.



ProQuest 10794289

Published by ProQuest LLC (2018). Copyright of the Dissertation is held by the Author.

All rights reserved.

This work is protected against unauthorized copying under Title 17, United States Code
Microform Edition © ProQuest LLC.

ProQuest LLC.
789 East Eisenhower Parkway
P.O. Box 1346
Ann Arbor, MI 48106 – 1346

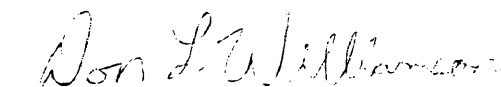
A thesis submitted to the Faculty and the Board of Trustees of the Colorado School of Mines in partial fulfillment of the requirements for the degree of *Master of Science (Materials Science)*.

Golden, Colorado

Date 6 / 9 / 97

Signed: 

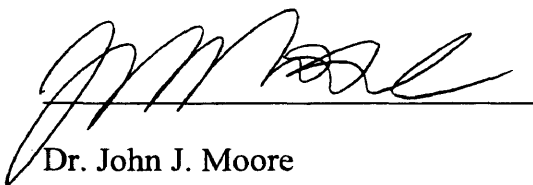
Nam Hyun Kang

Approved: 

Dr. Don L. Williamson
Thesis advisor

Golden, Colorado

Date 6/9/97



Dr. John J. Moore
Professor and Director,
Materials Science Program

ABSTRACT

In order to investigate the microstructural stability and hydrogen behavior in hydrogenated amorphous silicon-germanium alloys ($a - Si_{1-x}Ge_x:H$), systematic thermal annealing and small-angle x-ray scattering (SAXS) studies have been performed. The initial structures of as-deposited samples are not directly related to H or Ge contents, but to the deposition techniques. However, upon heat treatment the microstructures experience significant change depending on the H contents, Ge contents, and substrate temperature. Especially the microstructure depends on the H content due to the ability of H atoms to diffuse as a function of temperature in $a - Si_{1-x}Ge_x:H$, i.e., higher H samples experience lower microstructural stability through lower H stability. The weaker Ge-H bond than the Si-H bond leads to reduced microstructural stability. Finally, the H solubility depends on both the initial H content and Ge content. Even if H well above its solubility can be deposited with no detectable defects, the excess H is unstable and causes H complexes upon annealing. Annealing above 300°C induces the evolution of the excess H from the matrix and formation of H₂ spherical-like nanobubbles in the samples with 16 and 20 at. % H. The growing geometry of the nanovoids is dependent upon the preexisting microstructure.

TABLE OF CONTENTS

	Page
ABSTRACT .	iii
LIST OF FIGURES .	vii
LIST OF TABLES	ix
ACKNOWLEDGMENTS	x
Chapter 1. INTRODUCTION	1
1.1 Hydrogenated amorphous silicon-germanium ($a - Si_{1-x}Ge_x:H$) .	1
1.2 Purpose .	4
1.3 Approach .	4
1.4 Microstructural stability of hydrogenated amorphous silicon ($a - Si:H$)	6
1.4.1 Low-H content sample	7
1.4.2 High-H content sample	7
Chapter 2. SMALL-ANGLE X-RAY SCATTERING THEORY .	9
2.1 Scattering mechanisms .	9
2.1.1 Large-scale scattering ($I_L(q)$)	10
2.1.2 Inhomogeneity scattering ($I_N(q)$) .	11
2.1.3 Diffuse scattering (I_D)	14

2.2 Size and size distribution analysis	15
Chapter 3. SAMPLE PREPARATION AND EXPERIMENT	19
3.1 Sample preparation	19
3.2 SAXS system and procedure.	20
3.2.1 Description of SAXS system	20
3.2.2 SAXS data reduction procedures .	22
3.3 Annealing system and procedure .	23
3.4 Flotation density measurement .	26
Chapter 4. AS-DEPOSITED STATE OF $a - Si_{1-x}Ge_x:H$.	27
Chapter 5. MICROSTRUCTURAL STABILITY AND HYDROGEN SOLUBILITY UPON ANNEALING	34
5.1 General behavior of hydrogen and microstructural stability	34
5.2 Influence of substrate temperature (T_s) .	37
5.3 Influence of hydrogen	53
5.3.1 Low H content effects	53
5.3.2 High H content effects	55
5.4 Influence of germanium .	57
5.5 H stability and solubility .	59
5.6 Influence of initial microstructure	60
5.7 Tilting-effect	62

5.8. Time dependence .	64
Chapter 6. CONCLUSIONS .	68
REFERENCES.	72

LIST OF FIGURES

	Page
Fig. 1. Typical triple-layer solar cell structure	3
Fig. 2. The phase difference due to path difference OS between the waves from scattering centers O and P	10
Fig. 3. Spherical particle form factor $P^2(qx)$ as a function of qx .	17
Fig. 4. $x_i^2 P^2(qx_i)$ versus q .	18
Fig. 5. Schematic diagram of SAXS system at CSM	21
Fig. 6. Schematic diagram of (a) sample holder and (b) furnace	25
Fig. 7. SAXS intensity of as-deposited H samples .	28
Fig. 8. SAXS intensity of as-deposited U samples .	29
Fig. 9. SAXS intensity of as-deposited S samples .	30
Fig. 10. SAXS intensities of (a) H1 and (b) H2 upon annealing	38
Fig. 11. SAXS intensities of (a) U1 and (b) U2 upon annealing	39
Fig. 12. SAXS intensities of (a) S1 and (b) S2 upon annealing	40
Fig. 13. Integrated SAXS intensity Q upon annealing	41
Fig. 14. Diffuse scattering intensity I_D upon annealing	42
Fig. 15. Average radii of nanovoids $\langle R \rangle$ upon annealing .	43
Fig. 16. Density as a function of Ge content .	44

Fig. 17. XRD results of (a) H1 and (b) H2 as a function of annealing temperature .	45
Fig. 18. XRD results of (a) U1 and (b) U2 as a function of annealing temperature .	46
Fig. 19. XRD results of (a) S1 and (b) S2 as a function of annealing temperature .	47
Fig. 20. 45° tilted-SAXS intensity of (a) H1 and (b) H2	48
Fig. 21. 45° tilted-SAXS intensity of (a) U1 and (b) U2	49
Fig. 22. 45° tilted-SAXS intensity of (a) S1 and (b) S2	50
Fig. 23. Tilting effects as a function of annealing temperature	51
Fig. 24. Volume fraction of nanovoids as a function of annealing temperature	52
Fig. 25. Number density of nanovoids as a function of annealing temperature	52
Fig. 26. The size distribution of nanovoids for the S1 sample	54
Fig. 27. The size distribution of nanovoids for the H1 sample	58
Fig. 28. $\langle Q \rangle$ corrected by angular range from 0 to $\frac{\pi}{2}$	63
Fig. 29. Time dependence of the average volume change of particles for (a) S1 and for (b) H1 sample	67

LIST OF TABLES

	Page
Table 1. Summary of the six $a - Si_{1-x}Ge_x:H$ samples selected for this study	5
Table 2. The annealing treatment schedule	24
Table 3. Results of as-deposited SAXS analyses and flotation density	31
Table 4. Results of SAXS analyses of the H1 sample	56

ACKNOWLEDGMENTS

I would like to gratefully acknowledge Dr. Don L. Williamson, my thesis advisor, for two years of his confidence and advice. He led me to the right direction for practical approaches, and his guidance was very helpful for me to solve many problems and to emphasize the most valuable issues in this research project. Without his help and understanding, I could not have accomplished so much from this study.

I would like to thank Dr. Gerard P. Martins and Dr. Reuben T. Collins for contributing their time and energy while serving on my thesis committee.

The subcontract No. XAN-4-13318-04 from NREL is gratefully acknowledged for providing the financial support for this project.

Especially, I would like to thank my parents, who gave me this opportunity to start my career, for their moral and economical support. I would also like to thank my lovely sister, Julia, and my friends, Dae-Sun and Hyung-Suk, for their helpful advice. Finally, I thank the family of Korean Students Association for relieving my nostalgia and their kind concerns.

To my parents
and to recovery of my grandmother

Chapter 1

INTRODUCTION

1.1 Hydrogenated amorphous silicon-germanium ($a - Si_{1-x}Ge_x:H$)

Solar cells based on hydrogenated amorphous silicon ($a - Si:H$) have been studied since 1976 when Carlson and Wronski reported the first $a - Si:H$ solar cell [1]. Such cells are of interest because of the low production costs and adjustable band gaps by alloying. Furthermore these cells can produce power from an unlimited source and with less pollution compared with other methods such as gas or nuclear.

Present solar cells based on $a - Si:H$ have focused on multi-stacked junctions because single junction devices have not shown adequate efficiency and long-term stability. In order to collect a broader range of the solar spectrum, the solar cell is composed of tandem structures. Theoretical calculations of a top layer with a 2.0 eV band gap and a bottom layer with a 1.45 eV band gap have been executed in conjunction with a 1.7 eV $a - Si:H$ middle layer in triple junction devices to achieve a maximum conversion efficiency of 24 % [2]. For the low band gap layer, hydrogenated amorphous silicon-germanium ($a - Si_{1-x}Ge_x:H$) is presently the most promising material. Typical triple-layer solar cells depicted in Figure 1 are composed of hydrogenated amorphous silicon-carbon ($a - SiC:H$, $E_g = 2.1$ eV) or $a - Si:H$ with a great deal of hydrogen, $a - Si:H$ ($E_g = 1.7$ eV) and $a - SiGe:H$ ($E_g = 1.45$ eV) and they have up to 12.4 - 13.7 % initial conversion efficiency [3,4] for small areas (1 cm^2).

Hydrogen in $a-Si:H$ and $a-Si_{1-x}Ge_x:H$ plays an important role in assuring the good semiconducting properties by the removal of mid-gap states, i.e., by the saturation of dangling bonds. On the other hand, with the presence of hydrogen in the amorphous network, photo-degradation under prolonged illumination, which is known as the Staebler-Wronski effect [5], has been a major limitation in achieving stable properties. Furthermore, Ge or C incorporation in $a-Si:H$ reduces the effectiveness of hydrogenation, so that the $a-Si:H$ alloys with Ge or C become inferior photoelectronic materials. Such degradation by Ge alloying has been explained with diverse aspects, e.g., two-phase heterostructure [6], long-range electronic potential fluctuations [7], and inhomogeneous microstructural effects [8-11], as well as increases of dangling bond density [12-14]. These concepts help us to understand how photoconductivity decreases as x increases, i.e., more dangling bond states by increasing x induces positively-charged recombination centers for photo-generated carriers. These poor opto-electronic properties with the higher Ge contents ($x \geq 0.6$) are greatly improved by cathodic deposition [15].

In modern times, to improve the deposition speed for economical efficiency is a major goal for the deposition technique without degrading opto-electronic properties in comparison with the lower-deposition-rate method. By applying bias to the substrate during deposition, United Solar Systems Corporation (USSC) promoted ion bombardment of the surface to enhance the interactions on the surface, and greatly improved high-deposition-rate $a-Si_{1-x}Ge_x:H$ materials [16].

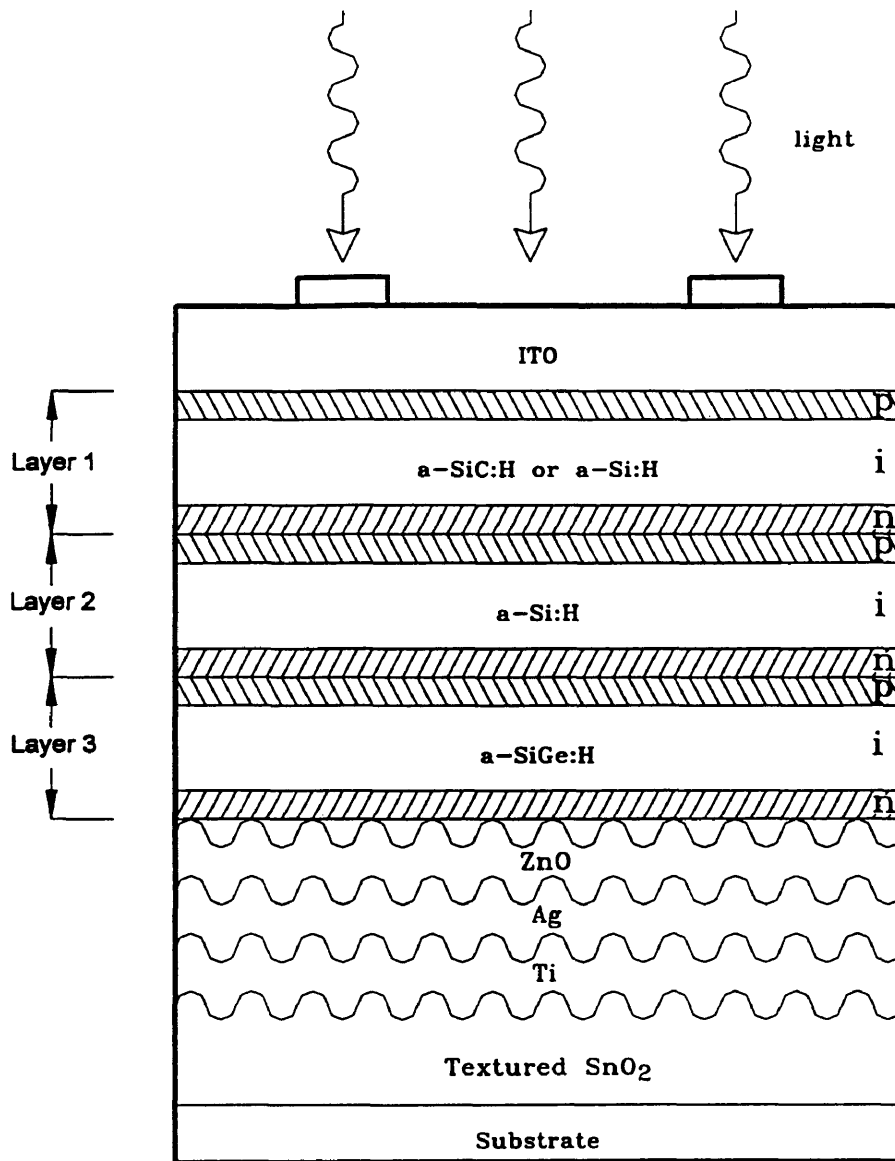


Fig. 1. Typical triple-layer solar cell structure
(Modified from reference 3)

1.2 Purpose

Microstructure and its connection with the hydrogen alloying require further investigation to understand its role in affecting the opto-electronic properties. Experiments that study the structure after annealing have provided useful information on the stability of the amorphous matrix and hydrogen clustering in $a-Si:H$ [17]. Very little of this type of work has been performed on $a-SiGe:H$ alloys. Does the weaker Ge-H bond lead to reduced structural stability? The goal of this research is to determine the microstructural stability of $a-Si_{1-x}Ge_x:H$ with respect to the Ge content, H content, and the initial microstructure by using the small-angle X-ray scattering (SAXS) technique.

1.3 Approach

In order to investigate the thermal stability of $a-Si_{1-x}Ge_x:H$ alloys, a carefully selected set of alloys with various Ge contents, H contents, and initial microstructures is subjected to a systematic annealing schedule. Prior SAXS research at CSM on the as-deposited structure of many $a-Si_{1-x}Ge_x:H$ alloys prepared by expert film makers from several groups allows the selection of a set of six samples for this study with the characteristics listed in Table 1.

Examination of data in Table 1 suggests the following possible correlations of thermal stability with as-deposited sample characteristics:

- (a) the effect of substrate temperature (T_s) during deposition via comparison of the S and H (low T_s) samples with the U (high T_s) samples;
- (b) the effect of Ge content via comparison of the S (low Ge content), U (mid-Ge), and H (high Ge) samples;

- (c) the effect of hydrogen content via comparison of the S and U samples (low hydrogen) with the H samples (high hydrogen);
- (d) the effect of initial microstructure via comparison of S1, U1 and H1 (low Q in which Q is defined as the indicator for the quantity of inhomogeneities in chapter 2) with S2, U2, and H2 (high Q), respectively.

Table 1. Summary of the six $a - Si_{1-x}Ge_x:H$ samples selected for this study

Sample	ID	x	H (at. %)	t (μm)	T_s ($^{\circ}C$)
Stuttgart H205111	S1	0.20	~ 6	2.8	200
Stuttgart H205191	S2	0.32	~ 6	2.9	200
USSC 2093	U1	0.54	~ 10	2.2	400
USSC 2092	U2	0.59	~ 7	3.3	400
Harvard 423	H1	0.70	20	2.7	200
Harvard 420	H2	0.75	16	2.5	200

It may be possible that one or more of these effects clearly dominates the thermal stability such that some of the effects are masked. A possible problem in the annealing process may be the interaction of the films with the Al substrate, leading to premature crystallization. Prior work has demonstrated the Ge on Al tends to inter-diffuse and

thereby induce crystallization at lower temperatures than Si on Al ($\cong 450^\circ\text{C}$) [18]. True crystallization temperatures are near 600°C (depending on Ge content). This interfering process is monitored by periodic x-ray diffraction of each sample.

The proposed detailed approach includes the following steps:

- (i) Remeasure the as-deposited SAXS of the S1 and S2 samples since these are already several years old and the SAXS system is now operating with increased data density versus scattering angle.
- (ii) Begin systematic annealing in steps of 25 - 50°C starting below the deposition temperatures (see Table 1). A detailed annealing procedure is described in section 3.3.
- (iii) Perform SAXS measurement after each anneal. Note any significant changes in Q and use this to make decisions regarding a time series study. Also use any large changes in Q to decide to measure x-ray diffraction.
- (iv) Continue the annealing process until limited by Al-substrate-induced crystallization.
- (v) Use all the data to establish the thermal stability of the microstructure and the hydrogen solubility in the set of alloys.

1.4. Microstructural stability of hydrogenated amorphous silicon ($a - \text{Si}:H$)

The role of H in $a - \text{Si}:H$ has been studied extensively and it may be helpful to understand the role of H in $a - \text{SiGe}:H$ which could be affected by the Ge content. The

following sections summarize briefly the work of Acco et. al. [17], especially the aspects of microstructural stability with H content. They studied the nanoscale structure by small-angle x-ray scattering (SAXS), the H evolution and solubility by secondary-ion mass spectroscopy (SIMS), and the H bonding behavior by infrared (IR) spectroscopy with hydrogen implanted *a-Si* samples subsequently annealed in steps from 200 to 550°C. Two types of samples were studied, one with a maximum H content 3 to 4 at. % and the other with a maximum of 20 at. % H.

1.4.1 Low-H content sample (3-4 at. % H)

The SAXS intensities indicated no angle dependence, which means no evidence of nanoscale defects related with H, during annealing up to 500°C. The diffuse intensity caused from the H alloying dropped after 300°C annealing, and it reached almost to the value of *a-Si* (i.e., no H) after 500°C. This decreasing diffuse scattering intensity as annealing temperature increases indicated H evolution as confirmed by SIMS H profiling.

1.4.2 High-H content sample (~20 at. % H)

This higher H content sample also showed angle-independent SAXS intensities up to 300°C anneal. Annealing above 300°C, the size and volume fraction of low-density nanoscale inhomogeneities increased with temperature, and interparticle interference effect due to a high density of inhomogeneities became significant. The intensity

decrease at the larger angles was matched with the evidence of the H evolution from the SIMS results. The growth of the inhomogeneities was attributed to precipitation of the H, which exceeded a solubility limit of 3 - 4 at. %, into nanobubbles containing H₂ molecules. Typical sizes of the nanobubbles were 2 to 3 nm and these features were confirmed by high-resolution transmission electron microscopy [19].

Chapter 2

SMALL ANGLE X-RAY SCATTERING(SAXS) THEORY

2.1 Scattering mechanisms

The SAXS signal is caused by the electron density fluctuations on the nanoscale such as microvoids or precipitates and on the atomic scale such as Laue monotonic scattering. There are also weak contributions from incoherent Compton scattering and thermal diffuse scattering.

Figure 2 illustrates that the x-ray scattering from a particle (electron density n_p) in a sample (electron density n_m) with λ (the x-ray wavelength) and 2θ (the scattering angle) can be defined as a function of the momentum transfer q (the difference of the wave vectors),

$$q = |\vec{k}_{out} - \vec{k}_m| = \frac{4\pi \sin \theta}{\lambda}, \quad (1)$$

where only the magnitude of q is needed if isotropic conditions are assumed.

From the SAXS signal versus q , the size and shape as well as the quantity of the particles can be characterized. To do this, the intensity from the scattering experiments can be divided into three contributions [20]:

$$I(q) = I_L(q) + I_N(q) + I_D. \quad (2)$$

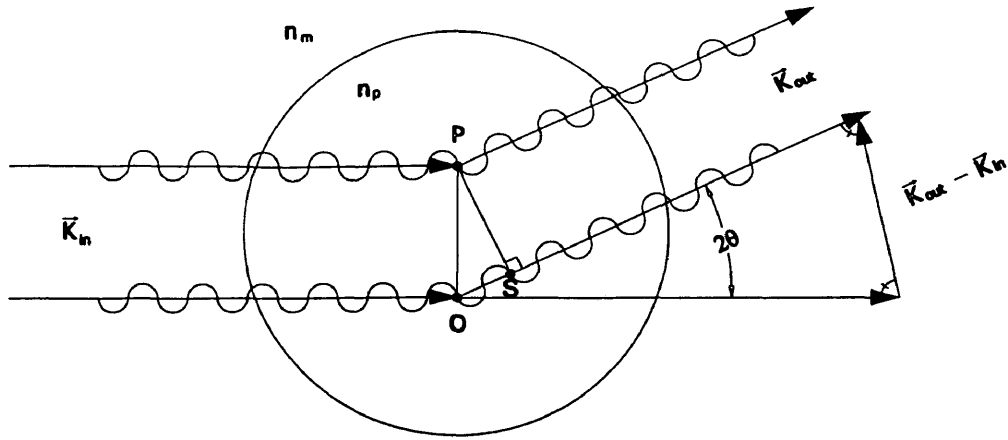


Fig. 2. The phase difference due to path difference OS between the waves from scattering centers O and P .

The details of these mechanisms will be developed in the following sections 2.1.1 - 2.1.3 based on three general references [21-23].

2.1.1 Large-scale scattering ($I_L(q)$)

The first term contributing to the SAXS intensity is from large-scale objects that can explain the low q part of the scattering curve by a well-known power-law (Porod's Law [21]), i.e.,

$$I_L(q) = Aq^{-s}, \quad (3)$$

$$I_L(q) = Aq^{-s}, \quad (3)$$

where A is a constant related to the total surface area of the objects. If the objects have sharp electron density boundaries for a point collimating system, the Porod exponent, s , has a value of 4. For slit collimation, this large-scale scattering can be expressed with the Porod exponent $s=3$, after correction for the effect due to a finite slit length. This intensity toward very low q may not be exclusively due to the objects in the bulk but also to the external sample surface [24].

2.1.2 Inhomogeneity scattering ($I_N(q)$)

$I_N(q)$ is of primary interest and represents the scattered intensity caused by the electron density fluctuations of nanostructural features such as voids on a scale from about 1 nm to about $\frac{\pi}{q_{\min}}$. Typically, $\frac{\pi}{q_{\min}}$ is about 30 nm in the slit geometry of CSM's SAXS apparatus. The observation of mass density deficits and other independent studies on $a-Si$ based thin-films, e.g., scanning tunneling microscopy (STM), nuclear magnetic resonance (NMR), and transmission electron microscopy (TEM) measurements [25-27], suggested for $a-SiGe:H$ material that a two-phase model of particles (i.e., microvoids) + amorphous matrix is valid. Under the isotropic assumption that the microvoids are spherical or, if non-spherical, that they are randomly oriented, $I_N(q)$ for a single particle

can be expressed in terms of a form factor, $P(qx)$, determined by the shape of the particle:

$$I_N(q) = CV^2(n_p - n_m)^2 P(qx)^2, \quad (4)$$

where C is a constant depending on choice of units, V and n_p are the volume and the uniform electron density of a particle, respectively, and n_m is the uniform electron density of a matrix [Fig. 2]. For the special case of a sphere with radius x , the form factor can be identified as:

$$P(qx) = 3 \left[\frac{\sin(qx) - qx \cos(qx)}{(qx)^3} \right]. \quad (5)$$

For a point collimating system, a useful scattering factor caused by nanostructural features is described as

$$Q \equiv \int I_N(q) q^2 dq = 2\pi^2 \Omega (n_p - n_m)^2 V_f (1 - V_f), \quad (6)$$

and for a slit collimating system to obtain higher counting rates in practice,

$$Q \equiv \left(\frac{q_s}{2} \right) \int I_N(q) q dq = 2\pi^2 \Omega (n_p - n_m)^2 V_f (1 - V_f), \quad (7)$$

where Ω is the average atomic volume of the sample, V_f is the volume fraction of the particles, and q_s is a geometrical factor controlled by the slit geometry [28]. Q in the above equations (6) and (7) is often called an “invariant” because Q is mainly dependent upon the mean square fluctuation of electron density with no impact from the detailed

structure of the particles, provided they are randomly oriented. Therefore the Q value is treated as a valuable factor in the SAXS experiment since it is the indicator for the quantity of particles in a sample, i.e. V_f .

For asymmetric particles of ellipsoidal shape, the measured V_f and Q values can be exaggerated if the particles are not randomly oriented. In reference [29], the approach to calculate the effective radius of x at a given direction is performed as a function of the short axis of a and the ellipsoidal aspect ratio ν :

$$x = a\sqrt{(\cos\alpha)^2 + (\nu\sin\alpha)^2}, \quad (8)$$

where α is the angle between the x-ray beam and the long axis. To explain the tilting effect and to acquire more quantitative V_f and Q values, the form factor $P(qx)$ needs to be corrected by substituting x of Eq. (8) into Eq. (5) and averaged over the angular range $\alpha = 0$ to $\frac{\pi}{2}$ under the assumption that all particles are ellipsoidal shape and oriented with the cylindrical axis perpendicular to the film surface.

Another effect that can occur and distort the shape of SAXS data is an interparticle interference effect due to a high density of particles. Particles close to one another can affect the scattering curve due to interference between scattered waves. Reference [30] explains one method for treating the observed $I_N(q)$ by introducing a hard-sphere pair correlation structure factor $S(qD)$ for hard spheres of diameter D .

2.1.3 Diffuse scattering (I_D)

I_D represents the diffuse intensity coming from several sources:

$$I_D = I_{LM} + I_{inc} + I_{TDS}, \quad (9)$$

where I_{LM} is the Laue monotonic scattering intensity, I_{inc} is the incoherent Compton scattering intensity and I_{TDS} is the thermal diffuse scattering intensity. Only the I_{LM} is strong enough to be relevant for this study and will be discussed in more detail. Information on I_{inc} and I_{TDS} can be found in other references [31-34].

The x-ray diffuse scattering known as Laue monotonic scattering is relevant for a sample consisting of more than one element. For a perfectly random solid binary solution $A_{1-x}B_x$, the Laue monotonic scattering intensity in electron units is

$$I_{LM} = (1-x)x(f_A - f_B)^2, \quad (10)$$

and for perfectly random ternary alloys $A_{1-x-y}B_xC_y$,

$$I_{LM} = (f_A - f_B)^2(1-x-y)x + (f_B - f_C)^2xy + (f_A - f_C)^2(1-x-y)y, \quad (11)$$

where x and y are the relative atomic concentrations respectively, f_A , f_B and f_C are the atomic form factors [35, 36]. For the SAXS measurement range ($0 < q \leq 6.2 \text{ nm}^{-1}$), the atomic form factors are almost equal to the atomic numbers Z_A , Z_B and Z_C .

If we let A = Si, B = Ge and C = H, then

$$I_{LM} = 324(1-x-y)x + 961xy + 169(1-x-y)y. \quad (12)$$

For example, if $x = 0.5$ and $y = 0.1$, $I_{LM} = 120$ eu. Noticeable deviations from this theoretical prediction may be attributed to short-range H clustering, vacancies, short-range Ge-Ge clustering in $a - SiGe:H$, or to significant differences in atomic volume of Si, Ge and H.

2.2 Size and size distribution analysis

The size and size distribution of particles causing the scattered intensity can be calculated under the following assumptions:

- (1) all particles have same shape;
- (2) the electron densities are constant in both the microvoids and the matrix;
- (3) the volume fraction of the particles is small, such that the interparticle interference effect is negligible.

Under these assumptions, the equations (1-7) are still effective for size distribution analysis. The scattered intensity from a distribution of scattering centers, particles, is given by [37]

$$I_N(q) = A \sum_i \omega(x_i) x_i^2 P^2(qx_i), \quad (13)$$

where $P(qx_i)$ is the form factor with characteristic radius x_i of a sphere, $\omega(x_i)$ is the volume fraction of the particles, and A is a constant indicating the total quantity of the

inhomogeneous particles.

The maximum value of $P^2(qx)$ is 1 at $qx = 0$, and $P^2(qx) = 0$ at $qx = 4.5$ as shown in Figure 3. In the region of $qx > 4.5$, $P^2(qx)$ fluctuates with a decreasing amplitude versus qx . Therefore mainly the smaller qx contribution provides the scattering intensity. Figure 4 explains the mainly contributing q regime in the curves of $x_i^2 P^2(qx_i)$ with different x_i . In this study, computer programs written by Williamson execute to fit a SAXS data set with up to 31 radii of spheres in the range from 0.4 to 10 nm, such that the average size and the size distribution of the particles can be obtained.

In order to obtain more quantitative data for the average size of particles, the observed $I_N(q)$ for the high H samples are fitted with a theoretical intensity function by introducing a hard-sphere pair correlation structure factor $S(qD)$ for hard spheres of diameter D [30]. To account for the interference effect,

$$I_N(q) = Ax^2 P^2(qx)S(qD), \quad (14)$$

is utilized for only one spherical radius x .

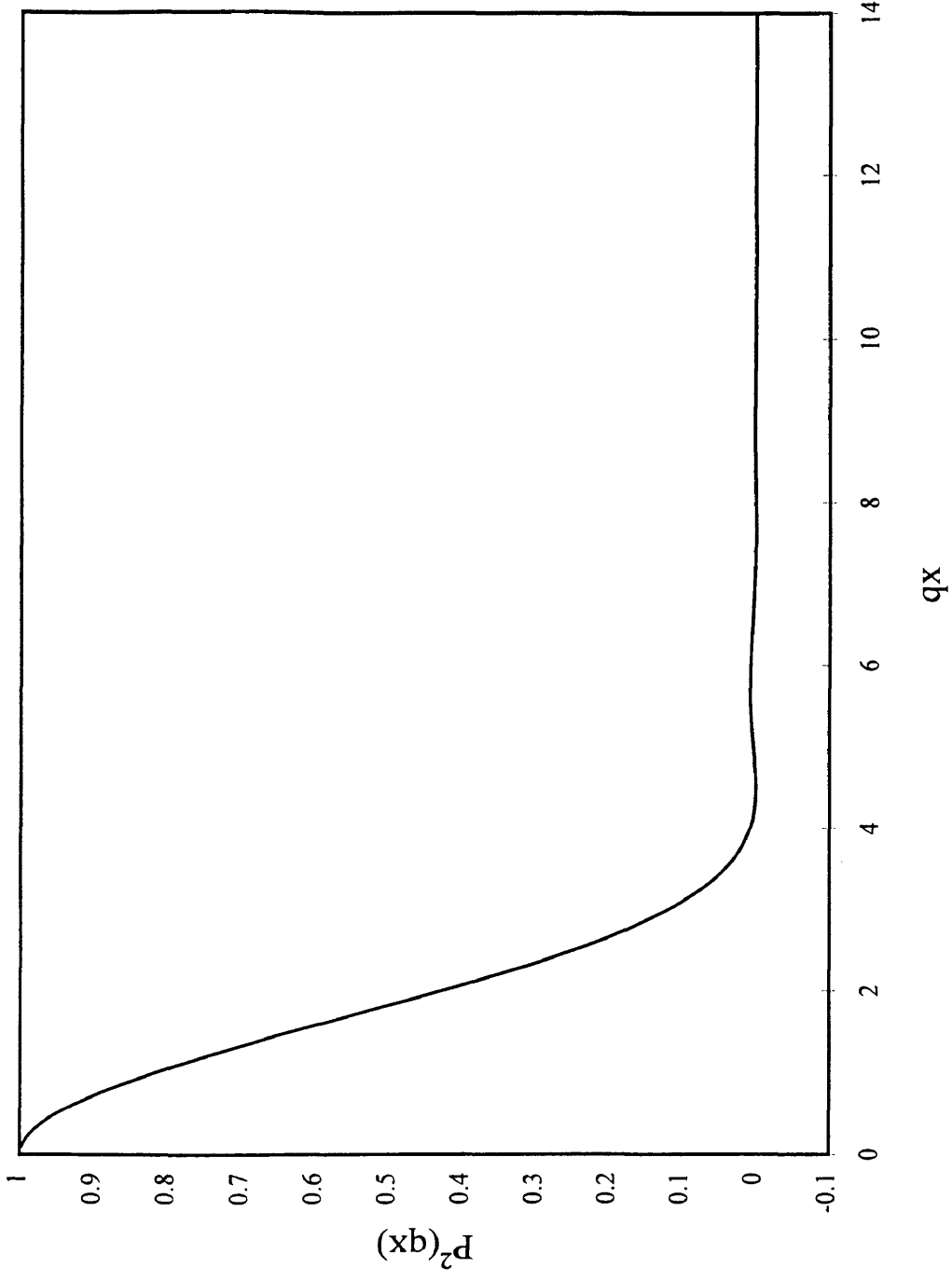


Fig. 3. Spherical particle form factor $P^2(qx)$ as a function of qx

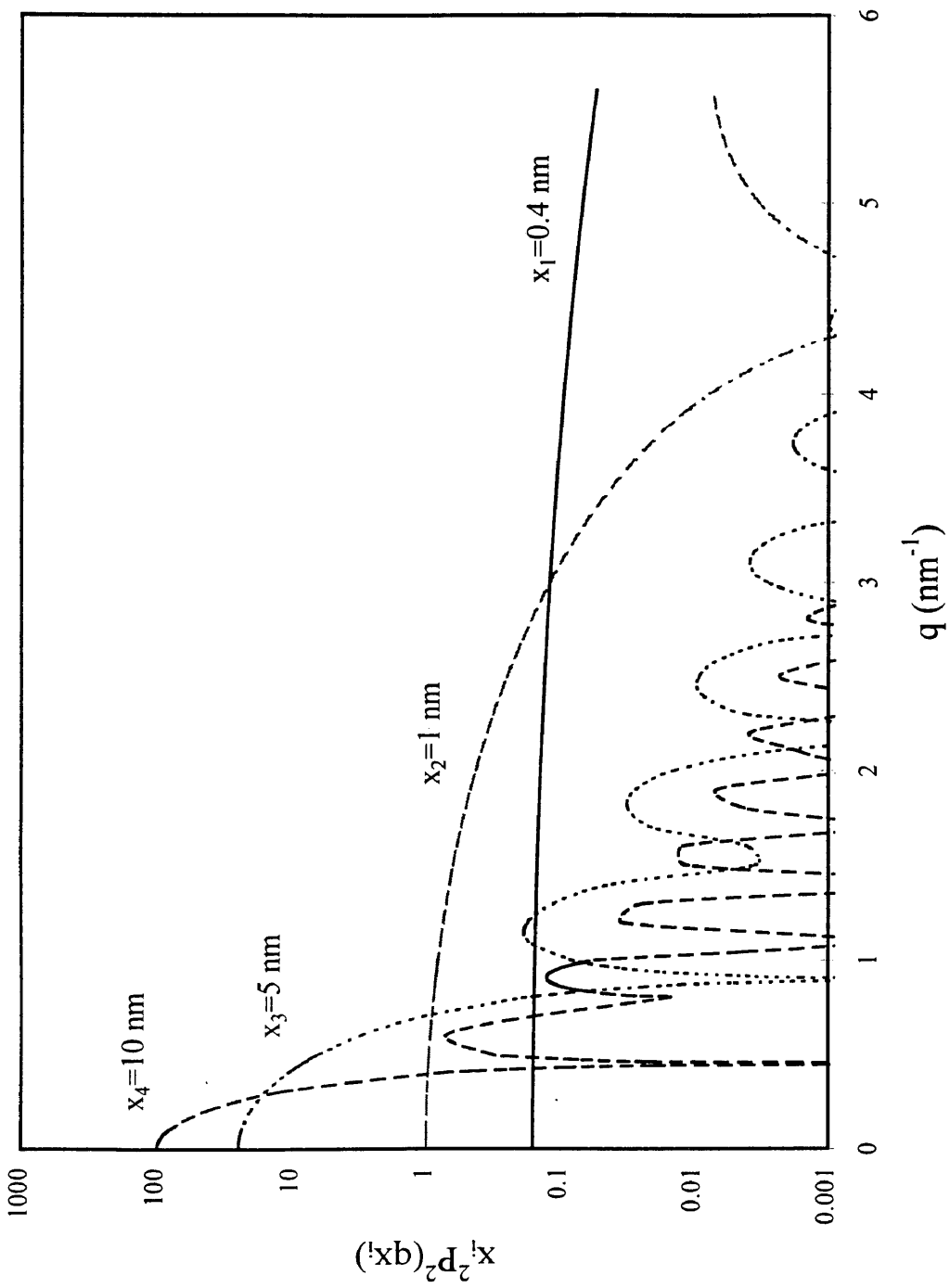


Fig. 4. $x_i^2 P^2(qx_i)$ versus q

Chapter 3

SAMPLE PREPARATION AND EXPERIMENTS

3.1 Sample preparation

The materials to be studied were prepared by three groups. The two samples with relatively low Ge content were fabricated at Universitaet Stuttgart using a dc glow discharge system. Films were deposited on a substrate of pure 10 μm -thick Al foil under the following conditions: GeH_4 and SiH_4 gas flows, T_s of 200°C, a chamber pressure of 0.34 mbar, a total gas flow of 30 sccm, an H_2 gas flow of 20 sccm, and a power density of $\approx 50 \text{ mW/cm}^2$ [9].

Samples with Ge content (x) near 0.5 were manufactured at United Solar Systems Corporation (USSC) by a microwave (MW) glow-discharge technique. Films were deposited on pure Al foil at high rates under the following conditions: GeH_4 and SiH_4 gas flows, frequency of 2.45 GHz, T_s of 400°C, pressure of 6 - 10 mTorr, and deposition rates of 4 nm/s with 60 V bias only for U1 sample [16].

High Ge content samples were deposited on the same type of pure Al foil substrates by plasma enhanced chemical vapor deposition (PECVD) at Harvard University under the following conditions: T_s of 200°C, pressure of 0.95 Torr, a power density of 1.2 W/cm^2 , an electrode spacing of 1.4 cm, GeH_4 and SiH_4 gas flows, an H_2

flow of 40 sccm, a rf signal frequency 13.56 MHz, yielding a cathode self-bias of -250V, and a growth rate of 0.8 nm/s. Deposition was on the powered cathode [15].

3.2 SAXS system and procedure

3.2.1 Description of SAXS system

The SAXS apparatus is a line-focus Kratky-type which utilizes x-rays from a Rigaku rotating Cu anode after passing through a graphite monochromator, as shown in Figure 5. The selected Cu- $K\alpha$ radiation ($\lambda = 0.15418$ nm) has a typical intensity at the sample of 1.5×10^8 photons/s with a beam of 0.13 mm x 14 mm cross section. The sample is folded into 7 layers to acquire enough sample thickness. Data are collected at pressures below 30 mTorr to minimize the air-scattering background and over a range in q from 0.09 to 6.2 nm^{-1} for about 10 - 13 hours by a predetermined stepmode scan.

The Ar-Xe gas filled proportional counter, which yields a low dark (absence of x-ray beam) counting rate of 0.16 /s, is used as a detector with a maximum efficiency of 90% for Cu- $K\alpha$ radiation. A useful feature of this SAXS system is that tilting effects associated with oriented nanostructure can be measured by changing the mounting angle (α) of the sample as illustrated in Figure 5, so that information on the shape of the scattering features can be obtained.

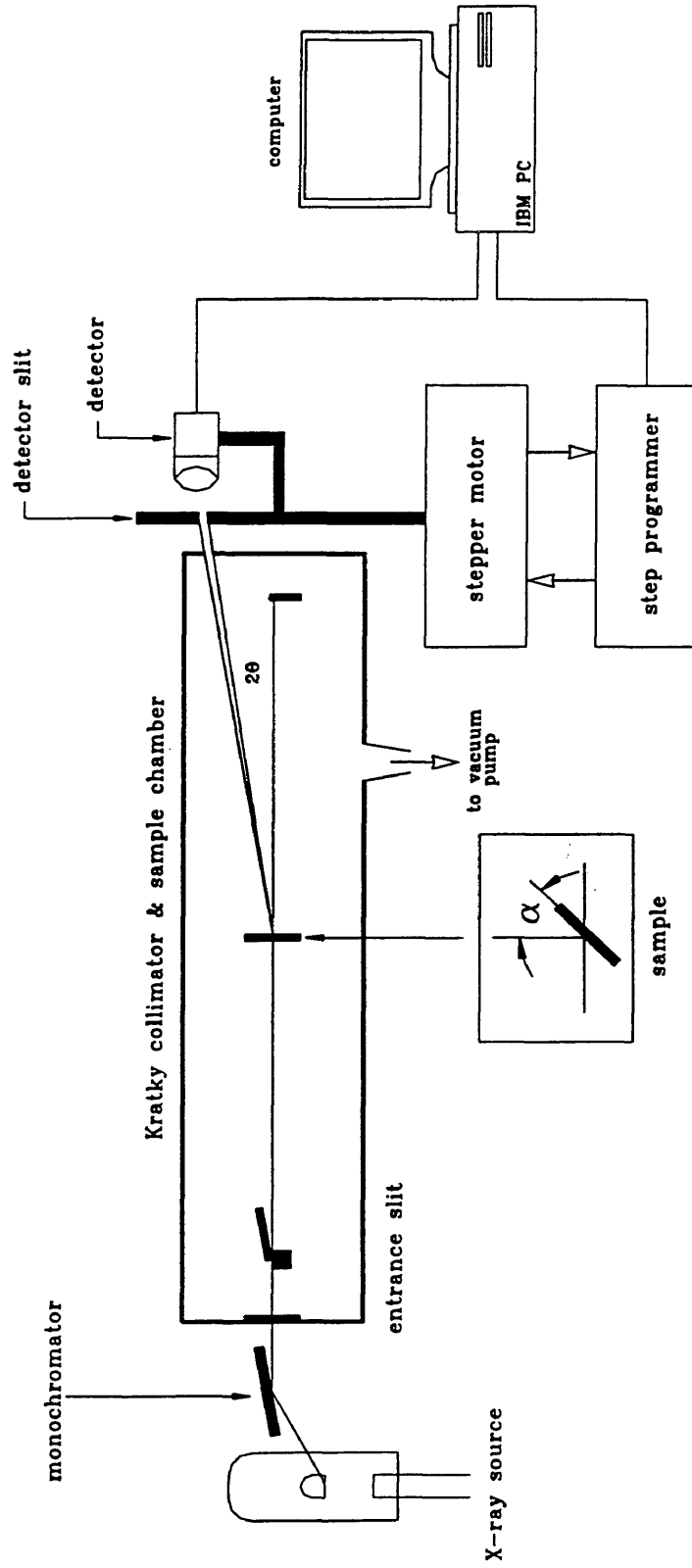


Fig. 5. Schematic diagram of SAXS system at CSM
(An insertion defines the tilting angle α) [Taken from ref. 38]

3.2.2 SAXS data reduction procedures

A careful data analysis procedure is then followed to remove substrate contributions from the raw SAXS data because all samples examined in this study are deposited on Al substrates of slightly different thickness ($\pm 10\%$). For linear drifts during the long scan times, the normalization of the incident x-ray intensity is necessary. Williamson et. al. [39] developed the equation for normalized intensity by using measurable quantities:

$$I_{norm}(q) = \frac{[I_m(q) - I_b] - [I_s(q) - I_b] \frac{P_{f+s}}{P_s}}{P_{f+s} \ln\left(\frac{P_s}{P_{f+s}}\right)} \quad (15)$$

where P_{f+s} and P_s represent the incident intensity attenuated by the sample (film + substrate) and the substrate, respectively, I_m is the measured SAXS intensity from sample, I_s is the measured SAXS intensity from substrate only, and I_b is the dark background count rate (0.16/s).

To compare the experimental intensity with theoretical values directly, the normalized intensity $I_{norm}(q)$ needs to be converted to absolute electron units (eu) or electrons/atoms (e/a). The intensity in electron units, $I(q)$, can be written as [38, 40]:

$$I(q) = I_{norm}(q) \frac{\mu\Omega a^2}{I_e A}, \quad (16)$$

where the parameters in the above equation are defined as follows:

μ = linear absorption coefficient of film (cm^{-1})

Ω = average atomic volume of the film

a = distance between sample and detector slit (20 cm)

I_e = square of classical electron radius ($e^2/mc^2 = 7.9 \times 10^{-26} \text{ cm}^2$)

A = area of the detector slit (0.0544 cm^2)

After these preliminary data procedures, the SAXS data interpretation by the theoretical processes described in chapter 2 is then followed to acquire information on the nanostructure in the sample.

3.3 Annealing system and procedure

To measure the microstructural stability, both the film deposited on Al substrate and the reference Al substrate are heat-treated for individual samples in a tube furnace. A furnace sample holder composed of a graphite boat and cover is used to hold the samples and the substrates, and it is specially designed to prevent surface oxidation of the samples during the annealing process. Figure 6 shows the sample holder, a schematic of the tube furnace and flow tube. After the sealed furnace is adjusted to the desired temperature, it is alternately evacuated and purged with He gas several times. High purity He gas is adjusted to a constant flow of 3 SCFH. Finally, the sample holder containing the samples

and substrates is pushed into the pre-stabilized temperature zone by using a thermocouple rod. It typically takes about 16 minutes for the sample holder to reach equilibrium. When the sample is pulled out of the hot zone of the furnace, it is still maintained under the flowing He atmosphere to prevent surface oxidation until $\leq 100^\circ\text{C}$.

The initial anneal time is one hour. If significant changes in the SAXS are noted for the one hour anneal, some time dependence is investigated through a series of anneals at the same temperature up to 16 or 32 hours. The times are selected based on a likely diffusion-controlled process, e.g., 1 hr, 2 hr, 4 hr, 8 hr and 16 hr. The actual annealing schedule used is listed in Table 2. Experiments were stopped after detection of significant crystallization.

Table 2. The annealing treatment schedule
(The numbers in each cell indicate the total annealing time at the designated temperature.)

Sample	200°C	250°C	300°C	350°C	375°C	400°C	425°C	450°C
S1	1	1	8	2	1	16	4	-
S2	1	1	8	2	1	16	4	-
U1	-	1	1	2	1	1	32	1
U2	-	1	1	2	1	1	32	1
H1	1	1	16	16	16	4	-	-
H2	1	1	16	16	16	4	-	-

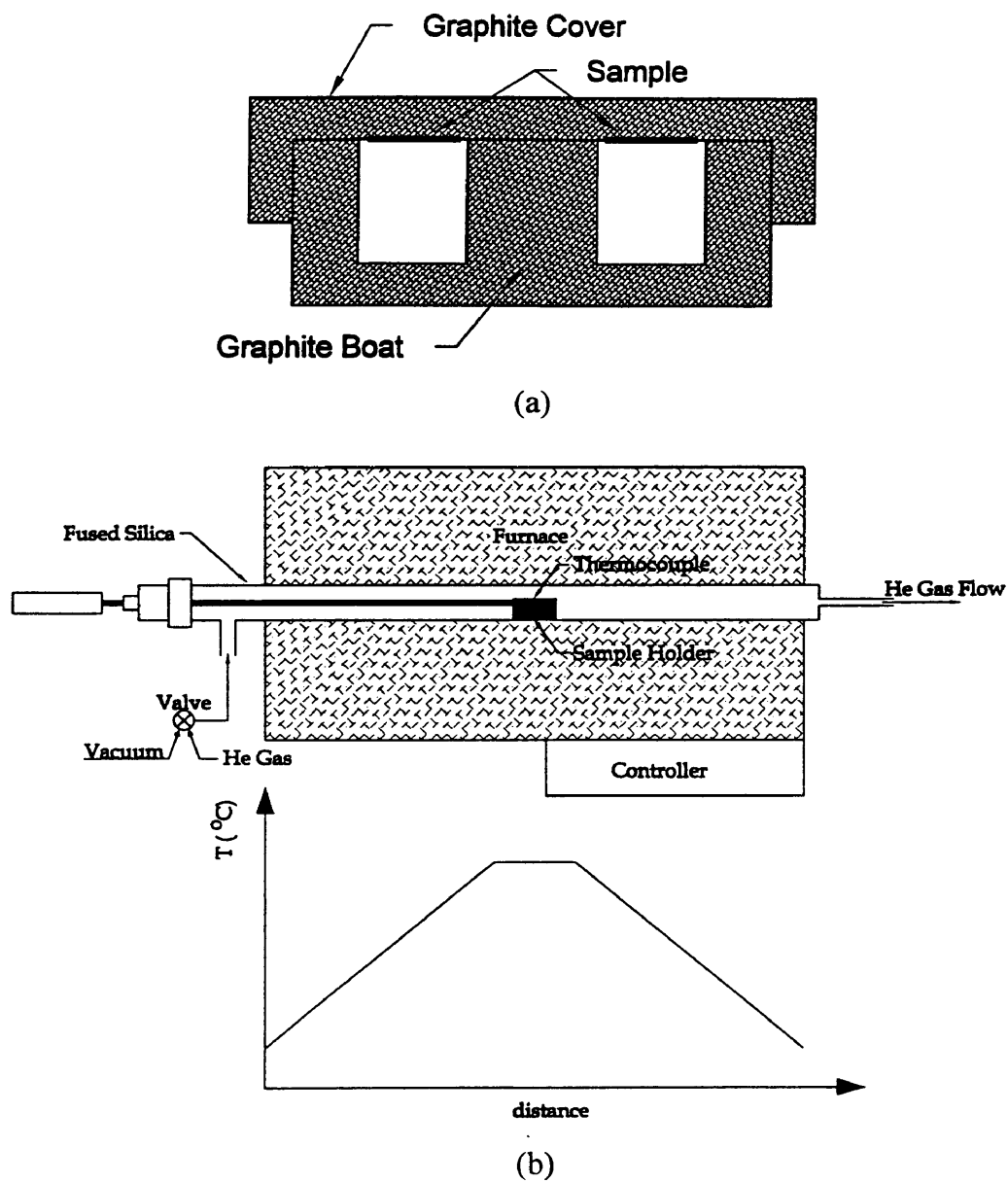


Fig. 6. Schematic diagram of (a) sample holder and (b) furnace
[Modified from reference 40]

3.4 Flotation density measurement

To identify low-density inhomogeneities acting as scattering particles in the SAXS intensity, a flotation density measurement is performed for $a - Si_{1-x}Ge_x:H$ samples. The Al substrate needs to be removed by etching in HCl + CuCl₂ solution in order to measure the density only of the film. After filtering the acid solution and sample onto filter paper, saturated thallium-malonate-formate solution and water are added until the film floats. The solution has a limit of 4.05 g/cm³, such that the density can be measured in $a - Si_{1-x}Ge_x:H$ material below $x \approx 0.6$. When the pieces of the sample properly float, the density (ρ) of the sample is calculated as:

$$\rho = 0.99542 \frac{W_{beaker+solution} - W_{beaker}}{2}, \quad (17)$$

where the constant of 0.99542 is the calibration factor determined for the 2 ml pipette by floating c-Si, $W_{beaker+solution}$ is the weight of the beaker filled with 2 ml of the thallium solution, and W_{beaker} is the weight of the beaker alone.

Chapter 4

AS-DEPOSITED STATE OF $a - Si_{1-x}Ge_x:H$

Figures 7-9 compare SAXS data from H1 and H2, U1 and U2, and S1 and S2, including the 45° tilting effect, for the as-deposited state. Table 3 lists the quantitative results from the analyses of these data. Since the $(Q_o / Q_{45})_N$ values are all greater than unity for S1, S2, U2, and H2 samples, it is clear that these samples have columnar-like structures with elongated features perpendicular to the surface. However, U1 and H1 samples have almost spherical features since the 45°-tilting curve is not much changed compared with no-tilting curve, although the $(Q_o / Q_{45})_N$ as well as Q cannot be determined because of the very small quantity of inhomogeneity. This shows that nearly homogeneous nanostructure can be obtained for the samples of high Ge or H contents by adjusting deposition conditions, although earlier studies [9, 41] showed if only Ge content was varied, more inhomogeneity occurred with a systematic increase in that one parameter.

Figure 7 shows that the optimized H1 sample has reduced SAXS intensity compared to the non-optimized H2 sample. The average size of the features $\langle R \rangle$, is quite small and smaller than the other samples (Table 3). At low scattering vectors, the curves show $q^{-3.2}$ and $q^{-3.3}$ power law behavior, respectively, which represent deviations from

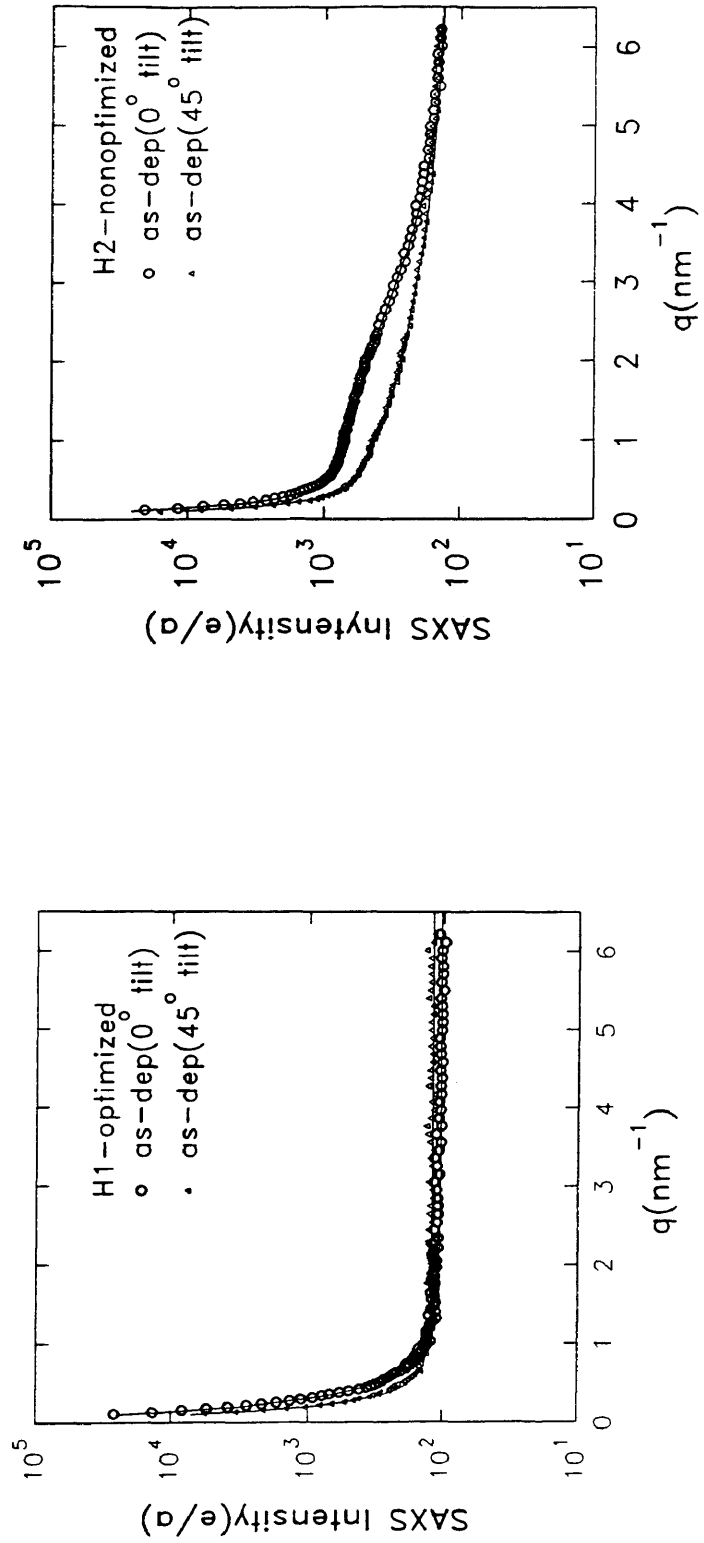


Fig. 7. SAXS intensity of the as-deposited H samples

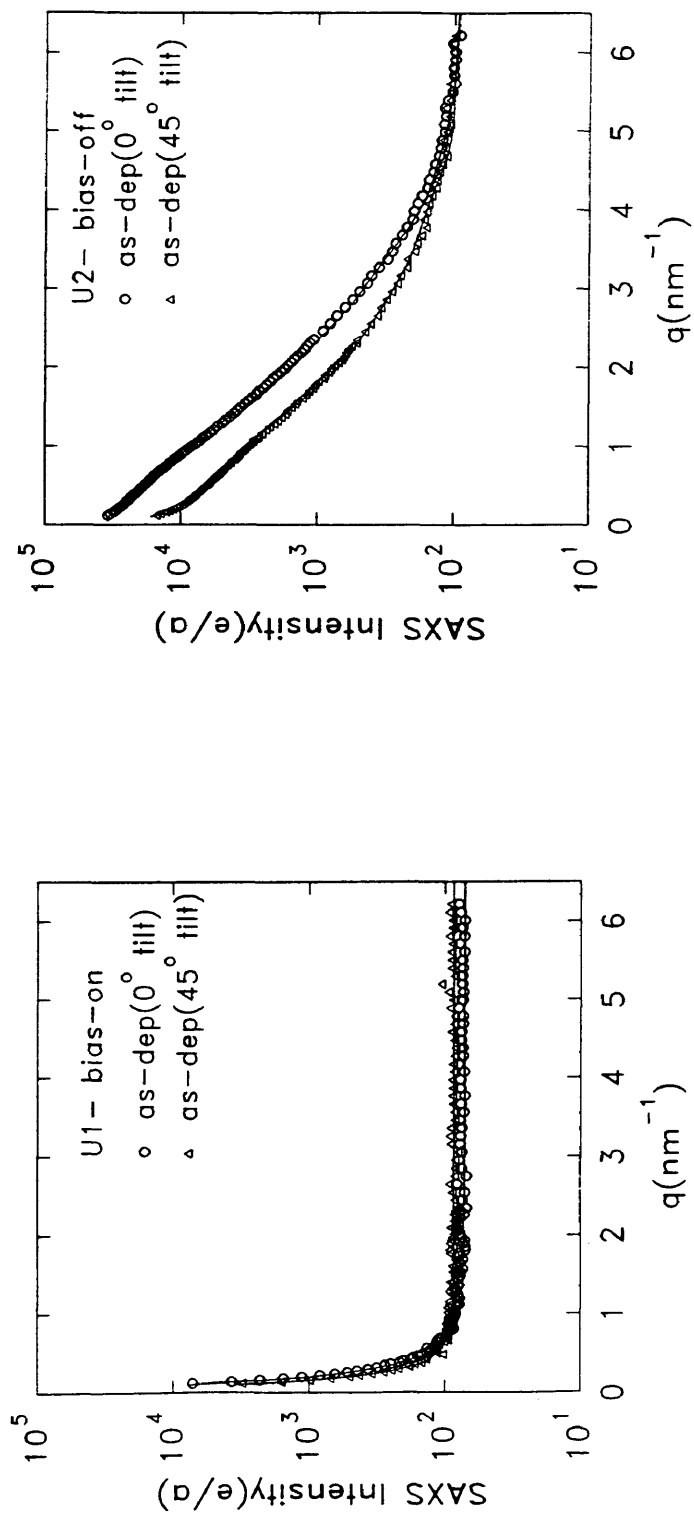


Fig. 8. SAXS intensity of as-deposited U samples

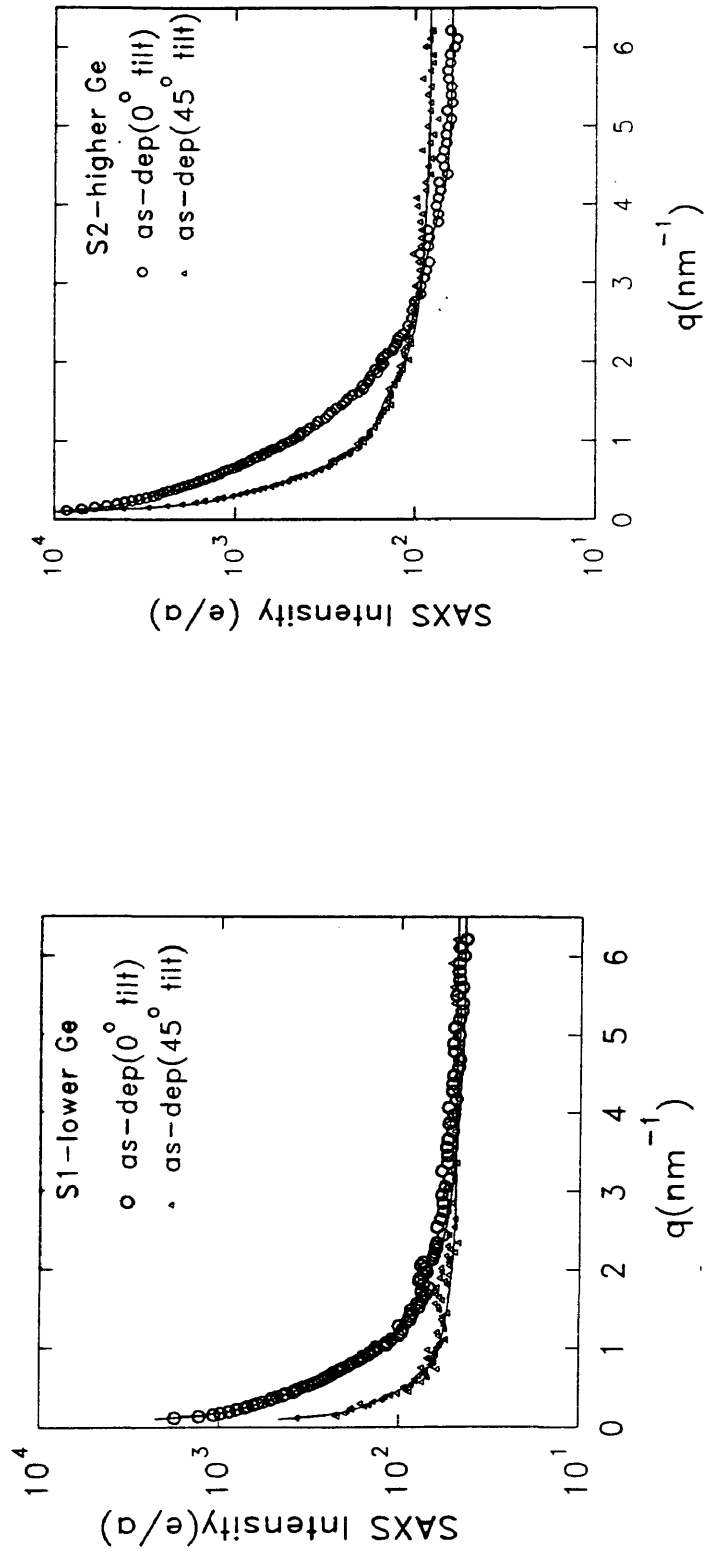


Fig. 9. SAXS intensity of as-deposited S samples

the q^{-3} Porod Law (Eq. (3)), perhaps indicating diffuse boundaries between the scattering particles and the $a - SiGe:H$ matrix [42].

Table 3. Results of as-deposited SAXS analyses and flotation density, where $(Q_o / Q_{45})_N$ is the ratio of Q obtained at 0° tilt angle compared to that at 45° , $\langle R \rangle$ is the average radius of the nanovoids, V_{f1} and V_{f2} are the volume fractions of the nanovoids from Eq. (7) by assuming zero and high-pressure of 0.2 GPa hydrogen electron densities, respectively, based on the reference 26, and $V_{f1,flot}$ is the density deficit calculated from the flotation density measurement at the as-deposited state. “a” indicates the estimated lower detection limit, and “b” unable to determine due to weak I_N signals.

Sample	Q (10^{24} eu/ cm^3)	$(Q_o / Q_{45})_N$	I_D (eu)	I_{LM} (eu)	$\langle R \rangle$ (nm)	V_{f1} (%)	V_{f2} (%)	$V_{f1,flot}$ (%)
H1	< 0.03 ^a	- ^b	102	159	- ^b	- ^b	- ^b	
H2	6	2.2	120	145	0.7	0.5	0.6	
U1	< 0.03 ^a	- ^b	73	119	- ^b	- ^b	- ^b	1.4
U2	38	2.5	75	109	1.7	3.5	4.2	7.2
S1	0.6	5.7	45	64	1.7	0.06	0.08	3.3
S2	2.62	3.4	60	86	2.1	0.33	0.41	3.3

From Figure 8 and Figure 9, the U1 sample deposited under applied bias and the S1 sample of smaller Ge content have much weaker SAXS intensity and therefore much lower volumes of micro-defects than the unbiased U2 sample and the S2 sample of larger Ge content, respectively. These results imply that ion bombardment induced from the

applied bias to the substrate during deposition causes more active surface mobility, such that the inhomogeneity is reduced dramatically. The larger Q for S2 sample was earlier associated with a microstructure transition above 20 % Ge [9]. All curves of S and U samples show q^{-3} behavior at low q , indicating a sharp interface between the scattering particles and the $a - SiGe:H$ matrix [42].

The H1 and H2 samples of high Ge and H contents show a higher diffuse intensity (I_D) than S and U samples as compared in Table 3 and Figures 7 - 9. This result is consistent with the calculations, I_{LM} , based on Eq. (12), but the experimental values are lower than the calculations by factors of 1.2 - 2.4. This implies that the hydrogen playing in a role of passivation of dangling bonds is either not entirely random in the $a - SiGe:H$ matrix and/or it is due to the atomic volume of hydrogen being small compared with Si and Ge [17]. Therefore the differences of I_D and I_{LM} values are more significant in higher H content samples, H1 and H2.

The flotation density is smaller than the crystalline density (Table 3) because of a combination of microvoids and the H alloying effect. The samples of lower Q show a smaller difference between the measured density and the calculated crystalline density due to less microvoids. The flotation density measurement for $a - SiGe:H$ alloys has a limit of 4.05 g/cm^3 , such that the flotation density of the high Ge content samples, H1 and H2, cannot be measured the flotation density.

Summarizing, the integrated intensity Q from the SAXS and the low-density inhomogeneity from the flotation density strongly depends on the deposition method rather than the H or Ge content effect. This can be seen clearly from the H1 sample of high H and Ge contents which has lower Q value than the S2 sample of low H and Ge contents; however, the H1 sample has higher Q than the S1 sample which has H and Ge contents similar to the S2 sample. The microstructural stability and hydrogen behavior is discussed in the following chapter 5.

Chapter 5

MICROSTRUCTURAL STABILITY AND HYDROGEN SOLUBILITY UPON ANNEALING

5.1 General behavior of hydrogen and microstructural stability

Figures 10, 11 and 12 show the SAXS intensity upon annealing for 1 hour in which the solid line indicates the fitted line with a theoretical distribution of spherical objects using Eq. (13) or (14). Generally, the SAXS intensity increases as the annealing temperature increases, i.e., the quantity of nano-scale inhomogeneity is increased. However, the U2 sample has a continuously decreasing SAXS intensity upon increasing the annealing temperature.

Based on the measured SAXS intensity versus q , the basic SAXS parameters obtained are:

- i) integrated SAXS intensity, Q (Figure 13);
- ii) diffuse scattering intensity, I_D (Figure 14);
- iii) average radii of nanovoids, $\langle R \rangle$ (Figure 15).

In these figures, the same group of samples is depicted with the same symbol, and the solid line is used for the low Q samples, i.e., H1, U1 and S1, to differentiate with the high Q samples, i.e., H2, U2 and S2. The vertical dotted lines correspond to

temperatures where a time series was initiated and all data between the lines was acquired at the temperature of the left dotted line. The series of data points versus time was always acquired in a doubling mode, i.e., 1h on the dotted line, then 2h, 4h, 8h, etc.

Q , indicating the quantity of nanovoids, is generally increased as the annealing temperature increases as Figure 13 shows, and this coincides with the increasing SAXS intensity from Figures 10, 11 and 12. Note the clear opposite behavior of Q from sample U2. This decreasing Q behavior for the U2 sample is confirmed by the flotation density measurement of Figure 16, in which the density after the last annealing step is larger than that of the as-deposited state. The S1 and S2 samples have decreased density upon annealing consistent with increased nanovoids. All samples experience slightly decreased Q at the last annealing temperature, and this result seems to have a connection with crystallization as based on the XRD results from Figures 17, 18 and 19. The decreased Q can be explained as due to the crystallization, returning atoms to positions of more stable potential energy, thereby reducing nano-defects causing the SAXS intensity. The larger density for the U1 sample after the last annealing step than that of the as-deposited state can be explained from this crystallization effect, i.e., the effect of increased nanovoids is not as large as the increased density effect caused by crystallization.

Figure 14 shows that I_D , the diffuse scattering intensity indicating H attachment in the amorphous matrix, is decreased upon annealing, and its drop coincides with the

increase of Q . The I_D curves appear as a maximum between 350°C and 375°C for U samples. This may be due to atomic-scale voids inducing the increase of I_D .

Figure 15 shows the average radius of nanovoids $\langle R \rangle$ as the annealing temperature increases. $\langle R \rangle$ is the average radius of the short axis perpendicular to the x-ray beam direction for ellipsoidal nanovoids calculated from the size distribution theory in chapter 2. To identify the shape of nanovoids, the SAXS intensity is measured with 45° tilting, such that generally reduced SAXS intensity is observed at 45° tilted measurement. Figures 20, 21 and 22 show the change of SAXS intensity between non-tilted and 45°-tilted orientations for the as-deposited state and after the last annealing step. Figure 23 compares the shape behavior of the nanovoids upon annealing, i.e., the closer $(Q_o / Q_{45})_N$ to unity, the more spherical-like shape of the nanovoids. Furthermore, the long axis parallel to the x-ray beam direction of the ellipsoidal nanovoids can be calculated from $(Q_o / Q_{45})_N$ data. Figures 24 and 25 show the volume fraction and the number density of the nanovoids, respectively, which can show the behavior of nanostructural inhomogeneity, e.g., nucleation or growth of nanovoids. A detailed discussion of the tilting effects is presented in section 5.7.

The microstructural stability and the hydrogen behavior are observed to be strongly dependent on the H and Ge contents upon annealing, even if the initial microstructure inferred from the SAXS intensity for high H or Ge content samples is much improved by adjusting the deposition methods. The following subdivided sections

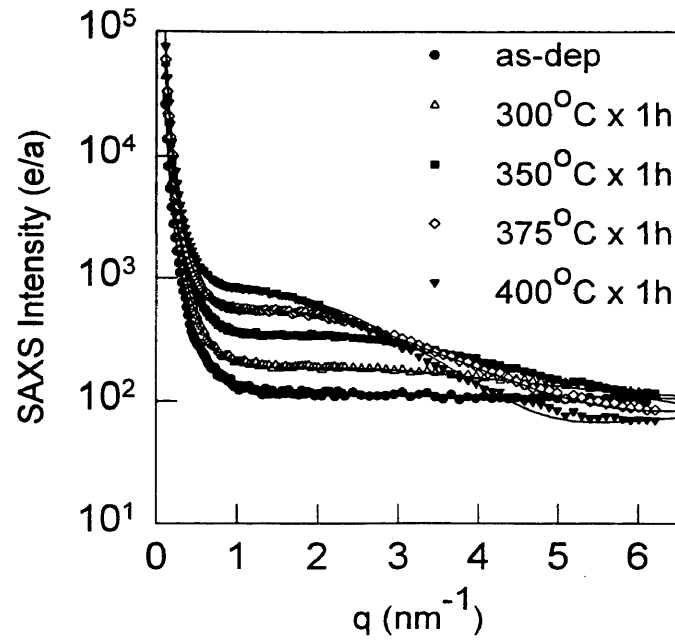
discuss the effects of deposition temperature, H content, Ge content, H solubility, initial microstructure, tilting, and time dependence.

5.2 Influence of substrate temperature (T_s)

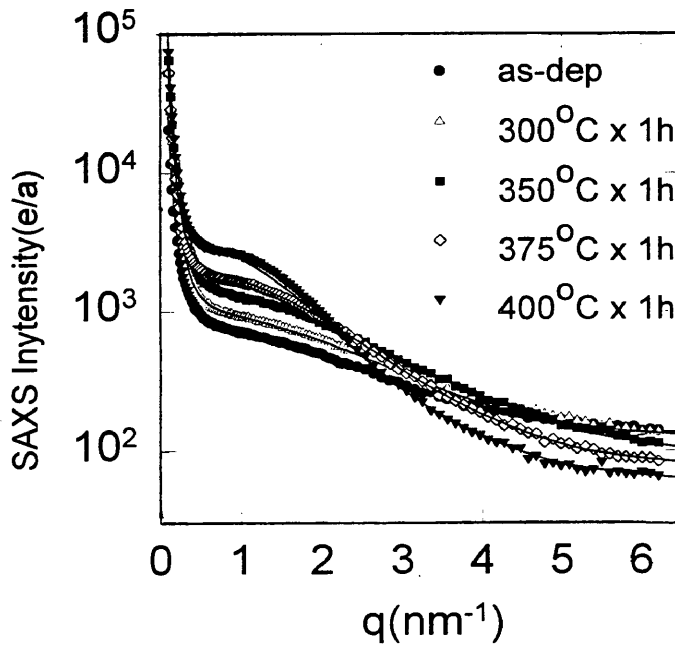
Figure 11 shows the SAXS intensities of high T_s samples, U1 and U2, as a function of annealing temperature. After examining the SAXS intensity and Q behavior from Figure 13 and comparing with Figures 11 and 12 for Low T_s samples, a simple connection of microstructural stability with T_s is observed.

The high T_s sample, U1, made under a bias to the substrate experiences a significant change of Q at $\geq 425^\circ\text{C}$ after nearly stable microstructure up to 400°C . However, the U2 sample deposited at the same temperature 400°C shows decreasing Q continuously from 250°C to 400°C , and finally its Q decreases significantly at $\geq 425^\circ\text{C}$. This is attributed to a metastable state created during the unbiased deposition at the high deposition rate of 4 nm/s. This metastability is clearly revealed by the changes induced below 400°C .

The low T_s samples, S and H, experience significant changes of Q beginning in the region of 250°C - 300°C , well above the 200°C deposition temperatures.

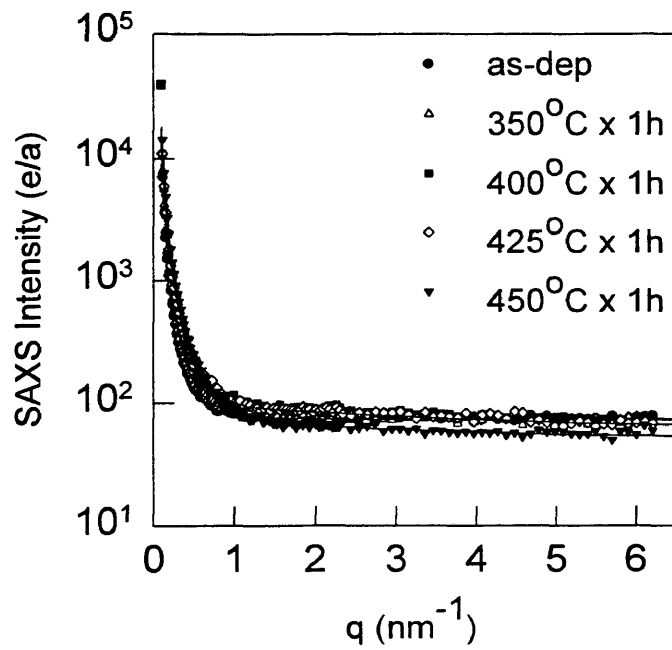


(a)

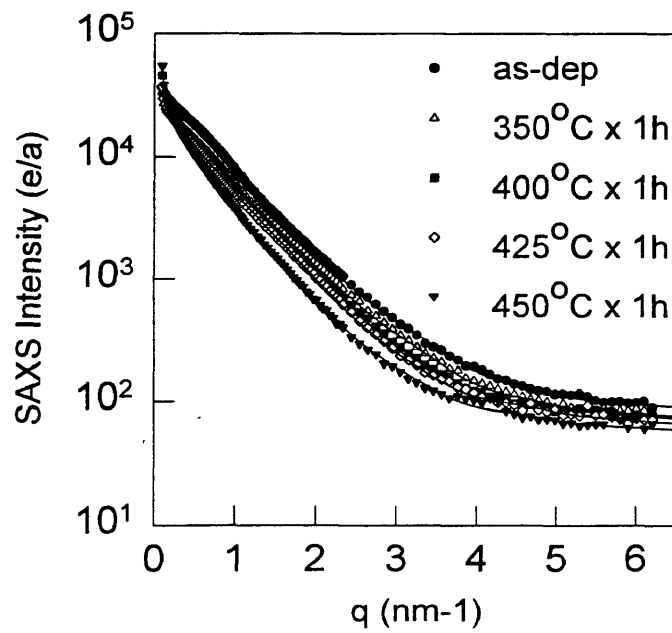


(b)

Fig. 10. SAXS intensities of (a) H1 and (b) H2 upon annealing

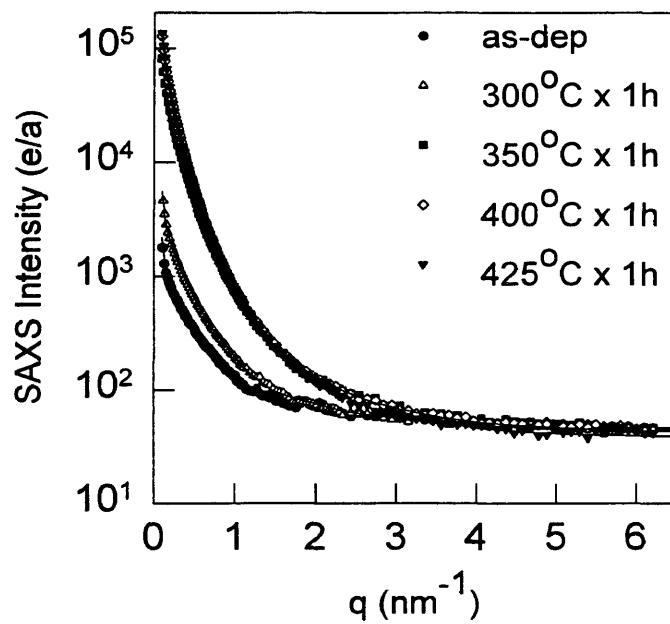


(a)

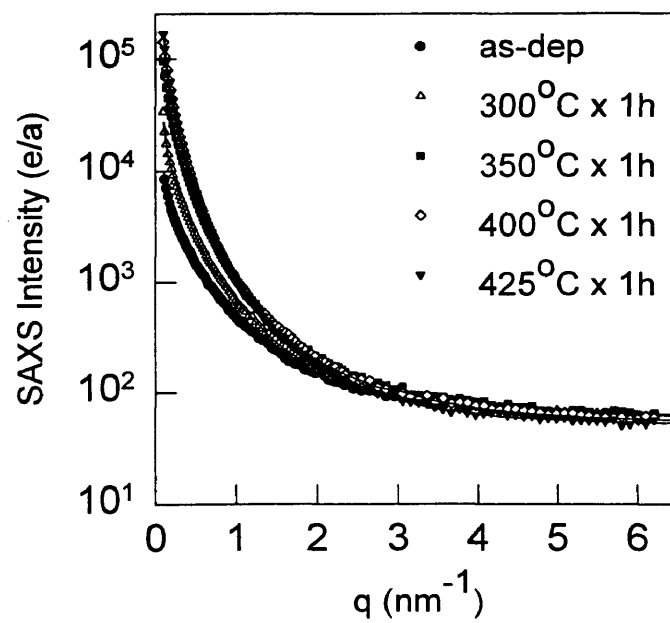


(b)

Fig. 11. SAXS intensities of (a) U1 and (b) U2 upon annealing



(a)



(b)

Fig. 12. SAXS intensities of (a) S1 and (b) S2 upon annealing

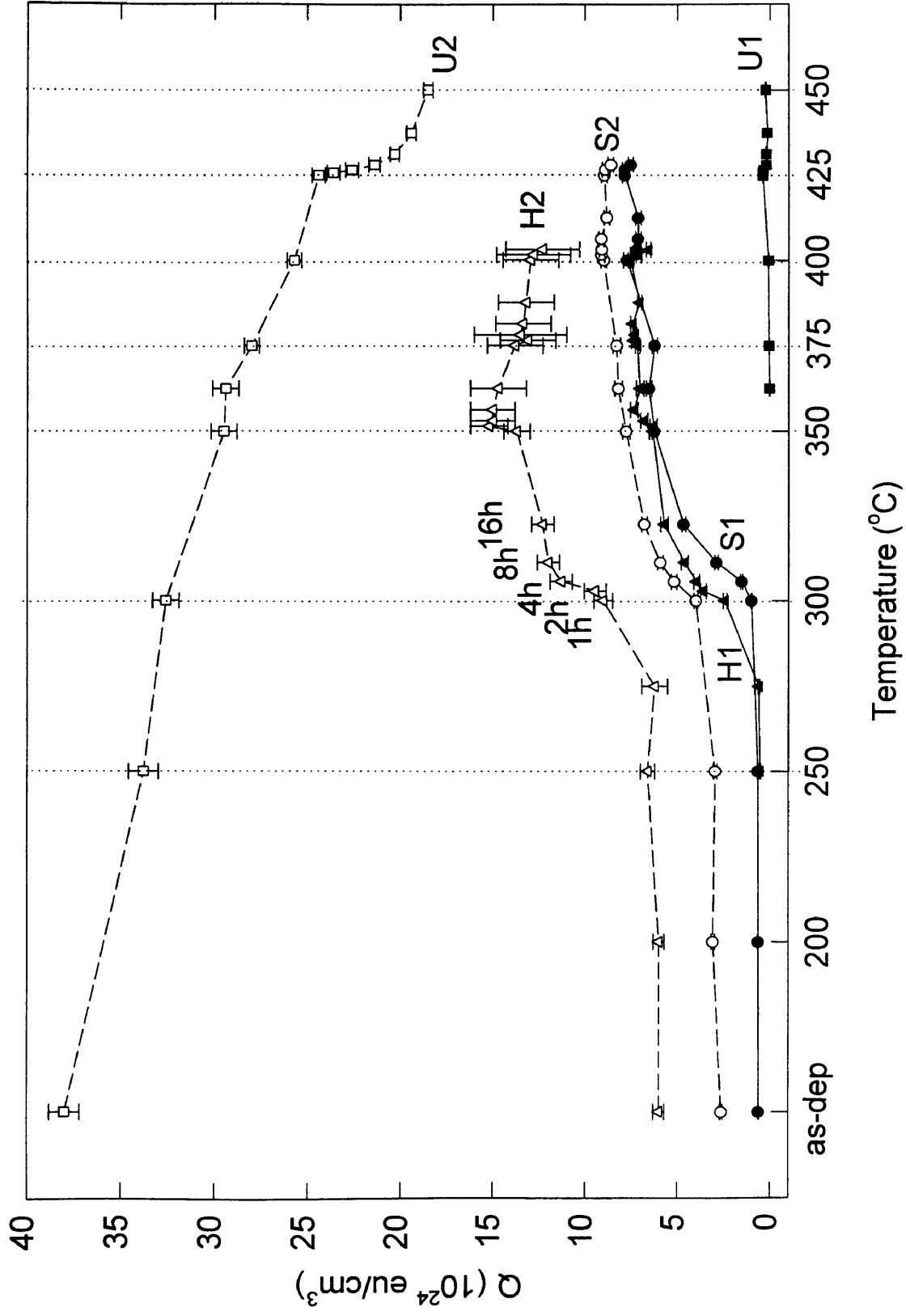


Fig. 13. Integrated SAXS intensity Q upon annealing

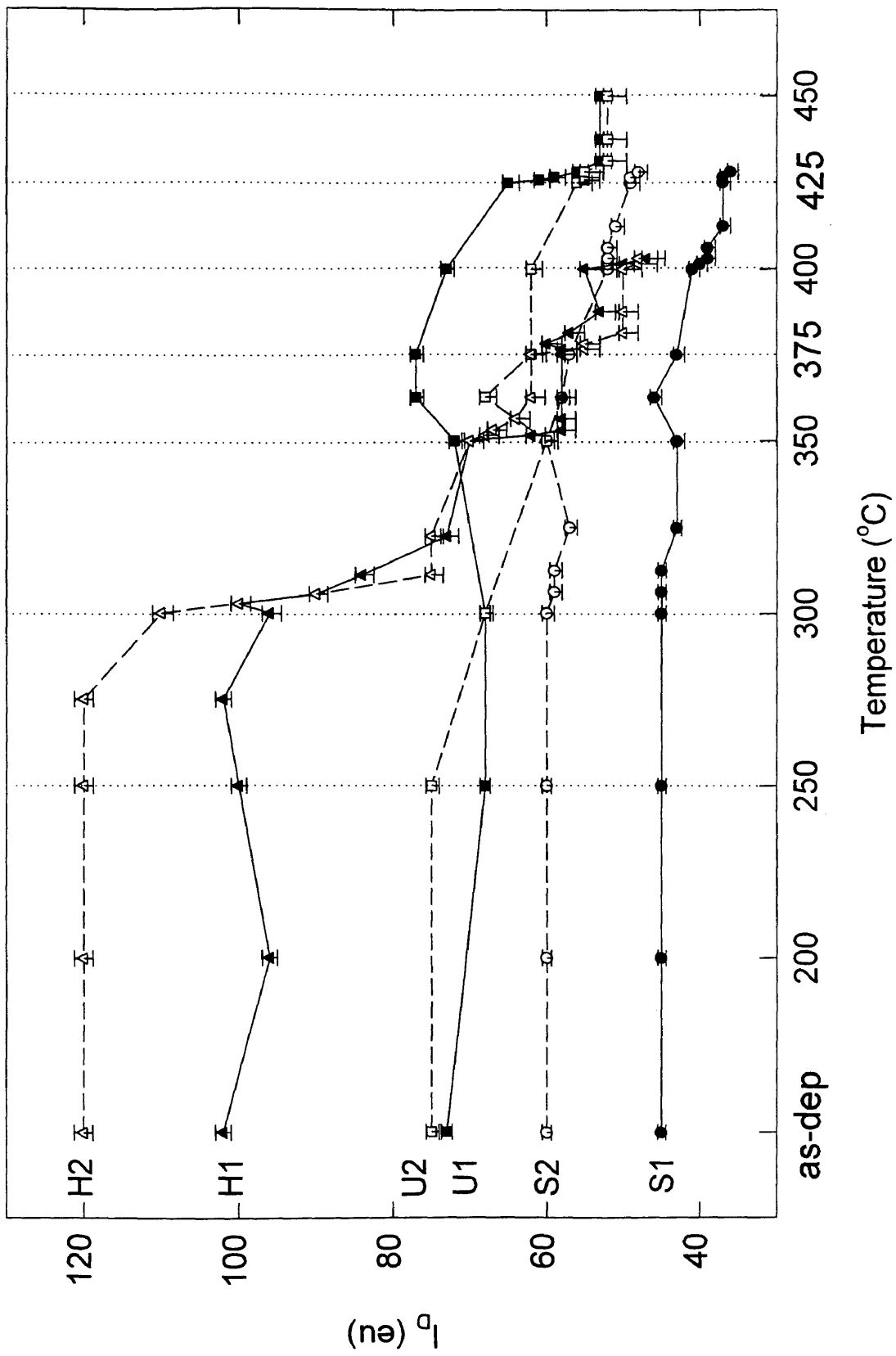


Fig. 14. Diffuse scattering intensity I_D upon annealing

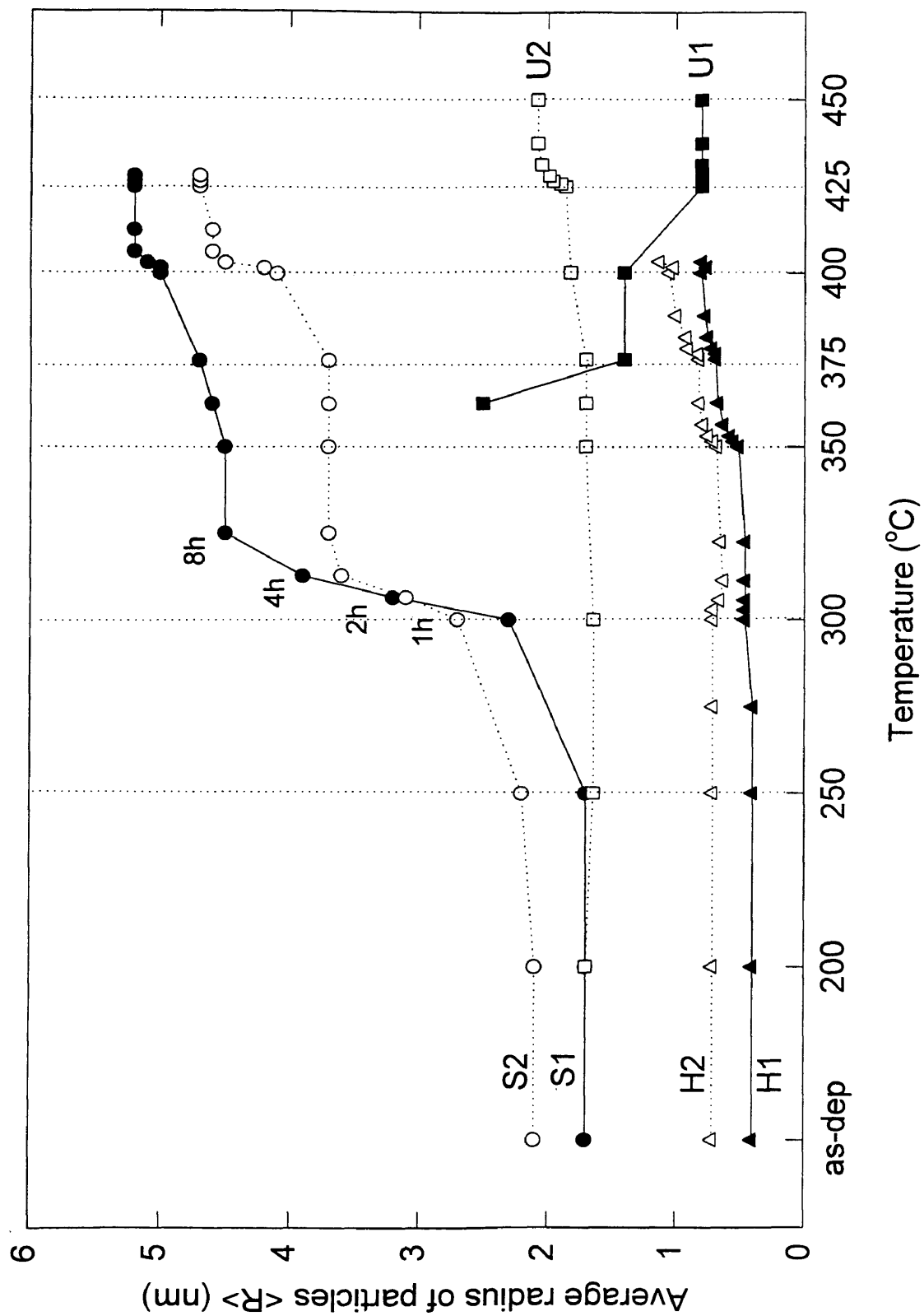


Fig. 15. Average radii of nanovoids $\langle R \rangle$ upon annealing

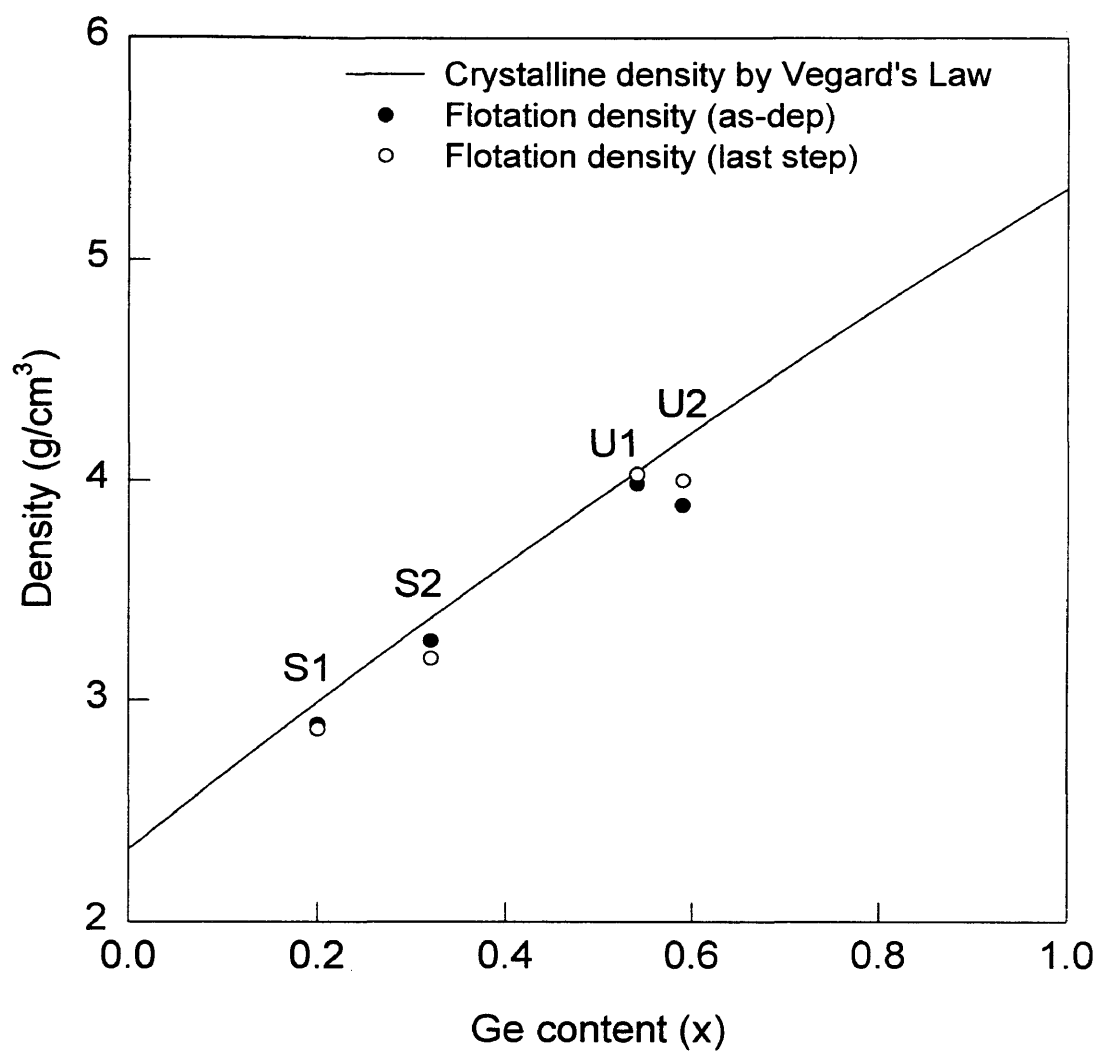


Fig. 16. Density as a function of Ge content

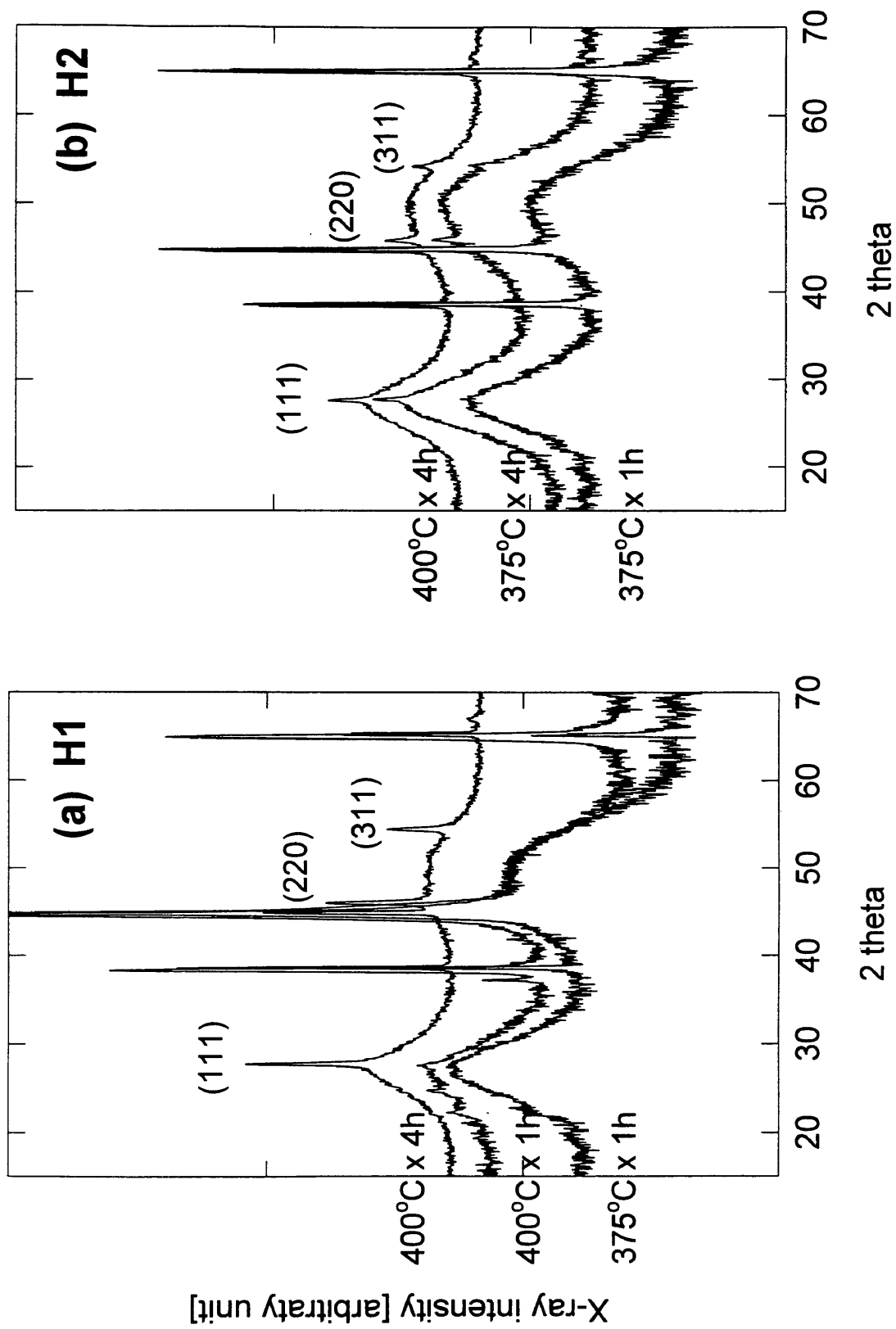


Fig. 17. XRD results of (a) H1 and (b) H2 as a function of annealing temperature

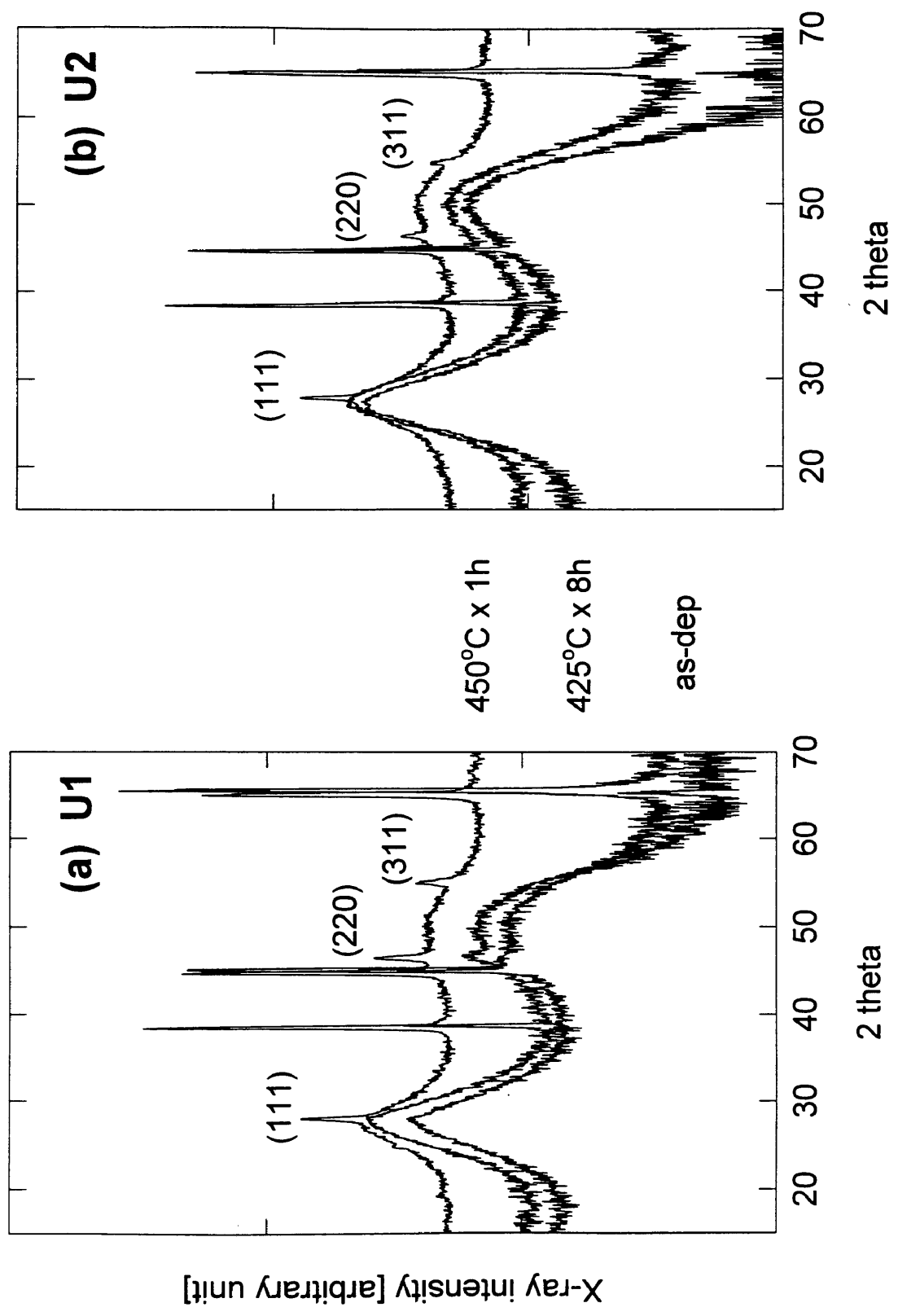


Fig. 18. XRD results of (a) U1 and (b) U2 as a function of annealing temperature

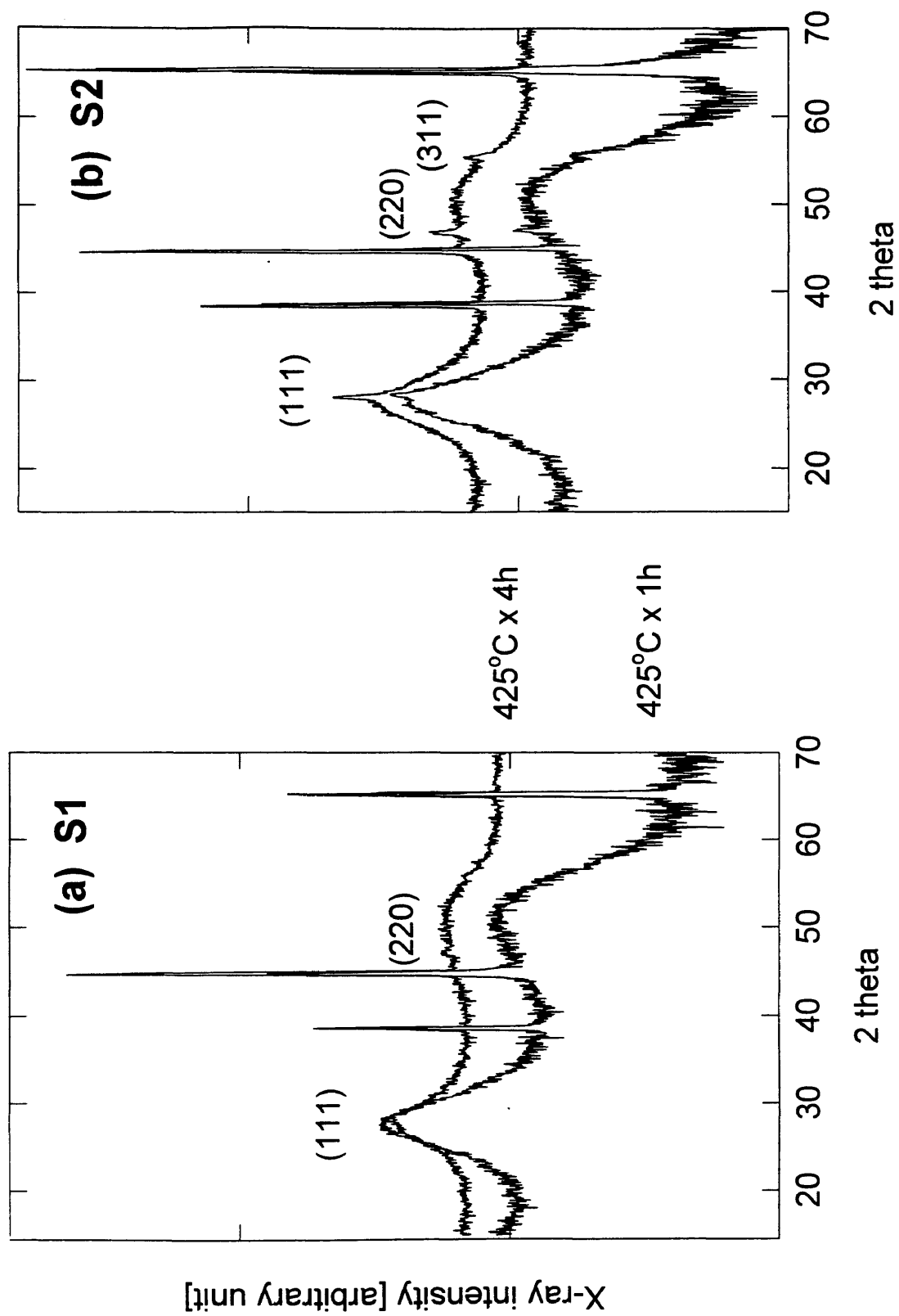
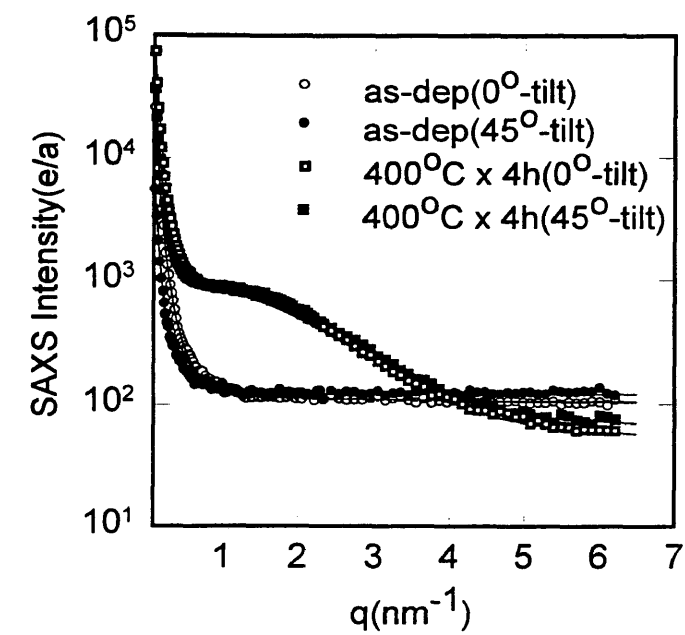
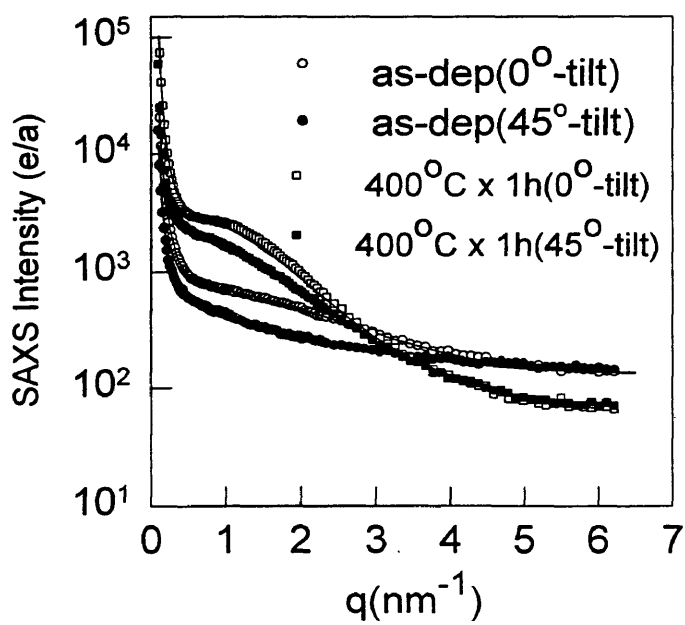


Fig. 19. XRD results of (a) S1 and (b) S2 as a function of annealing temperature

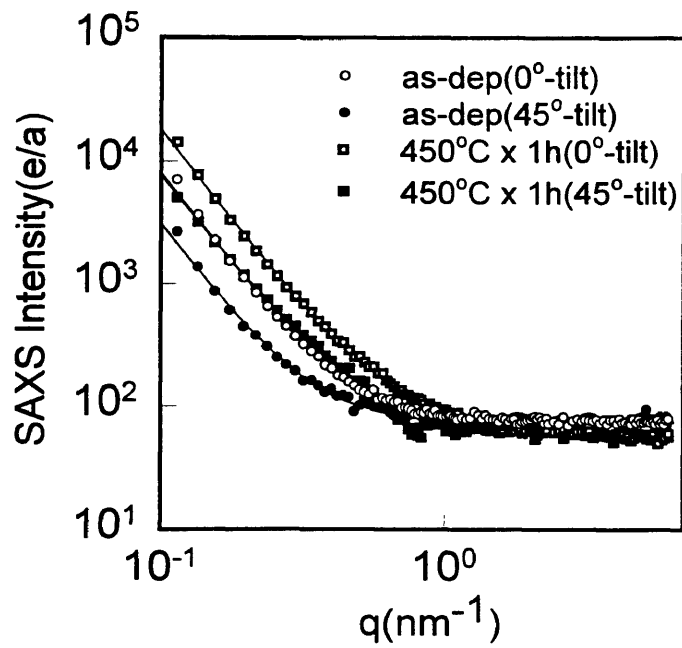


(a)

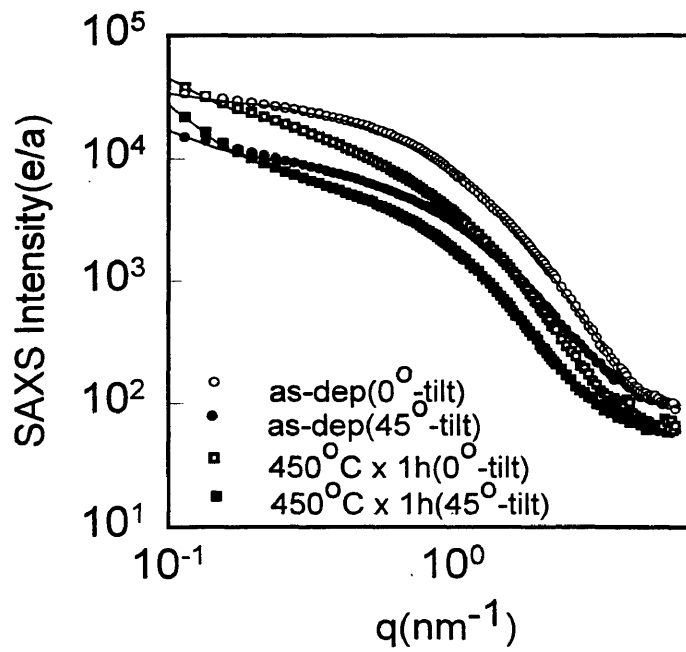


(b)

Fig. 20. 45° tilted-SAXS intensity of (a) H1 and (b) H2

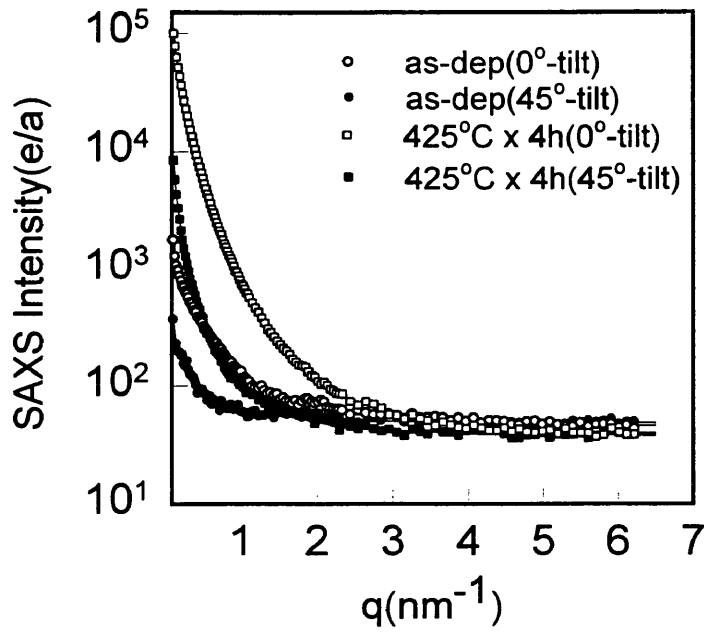


(a)

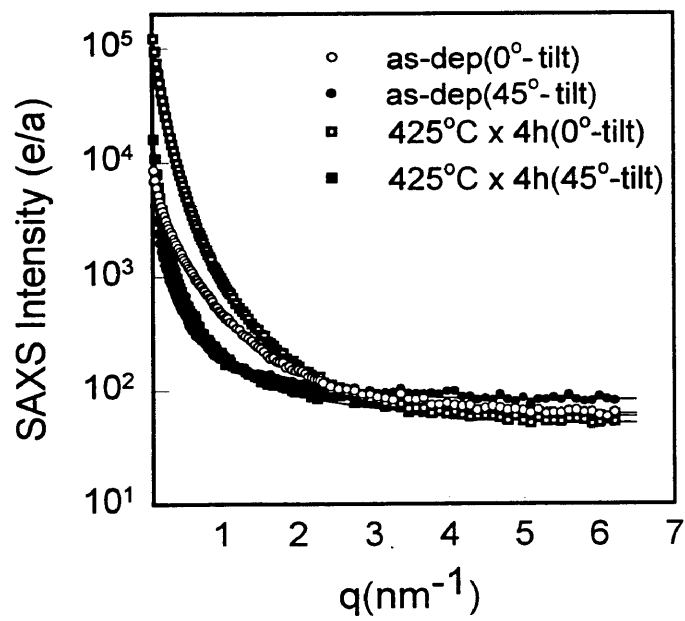


(b)

Fig. 21. 45° tilted-SAXS intensity of (a) U1 and (b) U2



(a)



(b)

Fig. 22. 45° tilted-SAXS intensity of (a) S1 and (b) S2

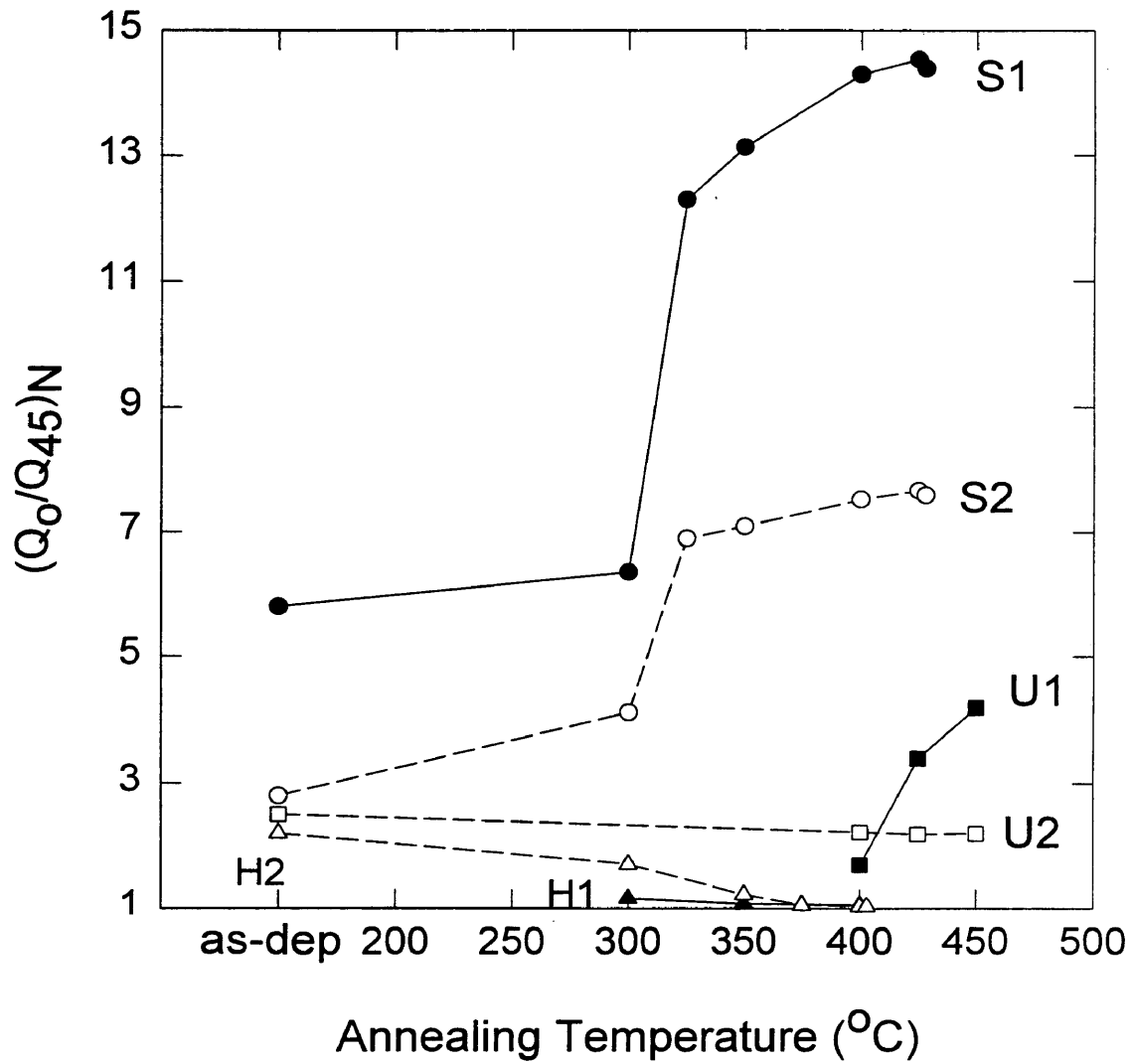


Fig. 23. Tilting effects as a function of annealing temperature

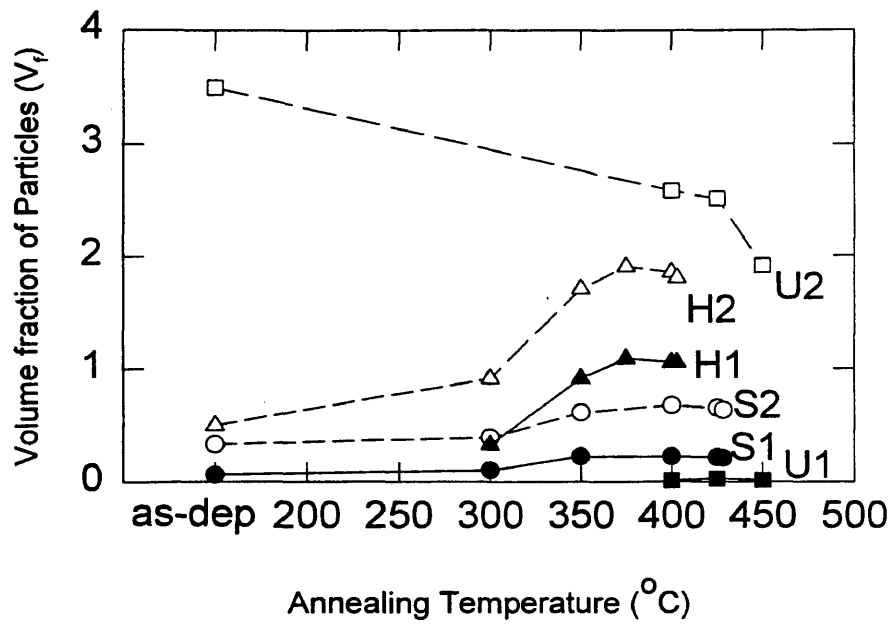


Fig. 24. Volume fraction of nanovoids as a function of annealing temperature

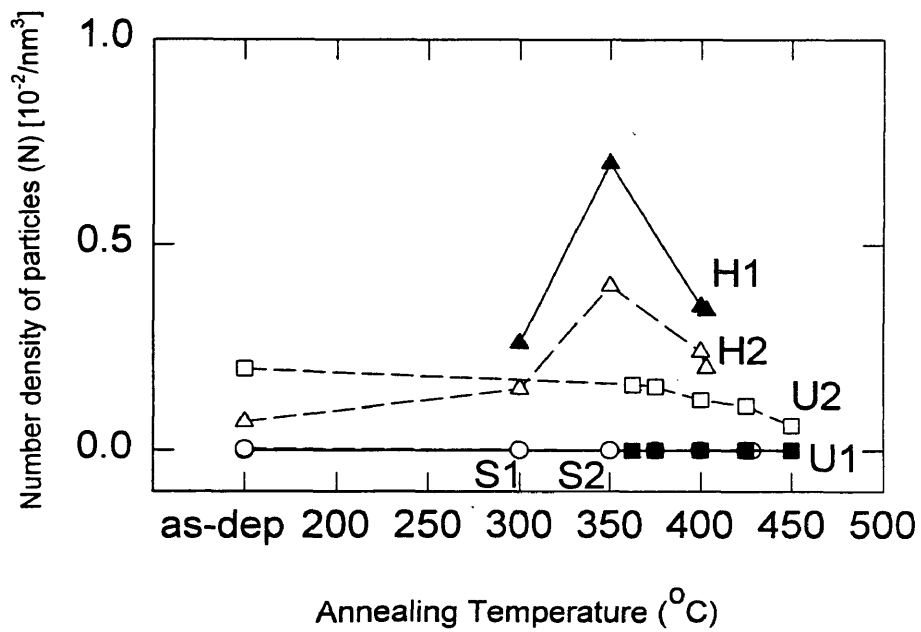


Fig. 25. Number density of nanovoids as a function of annealing temperature

5.3 Influence of hydrogen

Hydrogen can affect the annealing-induced microstructural changes in $a - SiGe:H$ alloys significantly because H can diffuse easier than Si or Ge atoms, and it is possible to form H complexes upon annealing, particularly if the solubility limit is exceeded. For this reason, H content causes a more significant difference in microstructural behavior rather than the effects of Ge or Si contents. Figures 23, 24 and 25 indicate the calculated volume fraction and number density of nanovoids with the measured $(Q_o / Q_{45})_N$ data to explain H effect. The following subsections are categorized into the low H samples (S1, S2) and the high H samples (H1, H2) and. U samples are excluded to prevent the effect of the substrate temperature.

5.3.1 Low H content effects

Figure 12 shows the SAXS intensities from the S samples in the as-deposited state and after annealing for 1h at different temperatures. Annealing at 200°C and 250°C cause very little change in the SAXS intensity, and above 300°C there are systematic increases with elongated geometry of the low-density particles as confirmed from Figure 23. Even if the volume fraction of voids is increased with increasing temperature, the number density is decreased because their average sizes are significantly increased as indicated in Figure 15. After the 250°C annealing the average dimensions for S1 is about 4 x 42nm (minor x major axes), but it is increased to about 10 x 272 nm after 425°C annealing

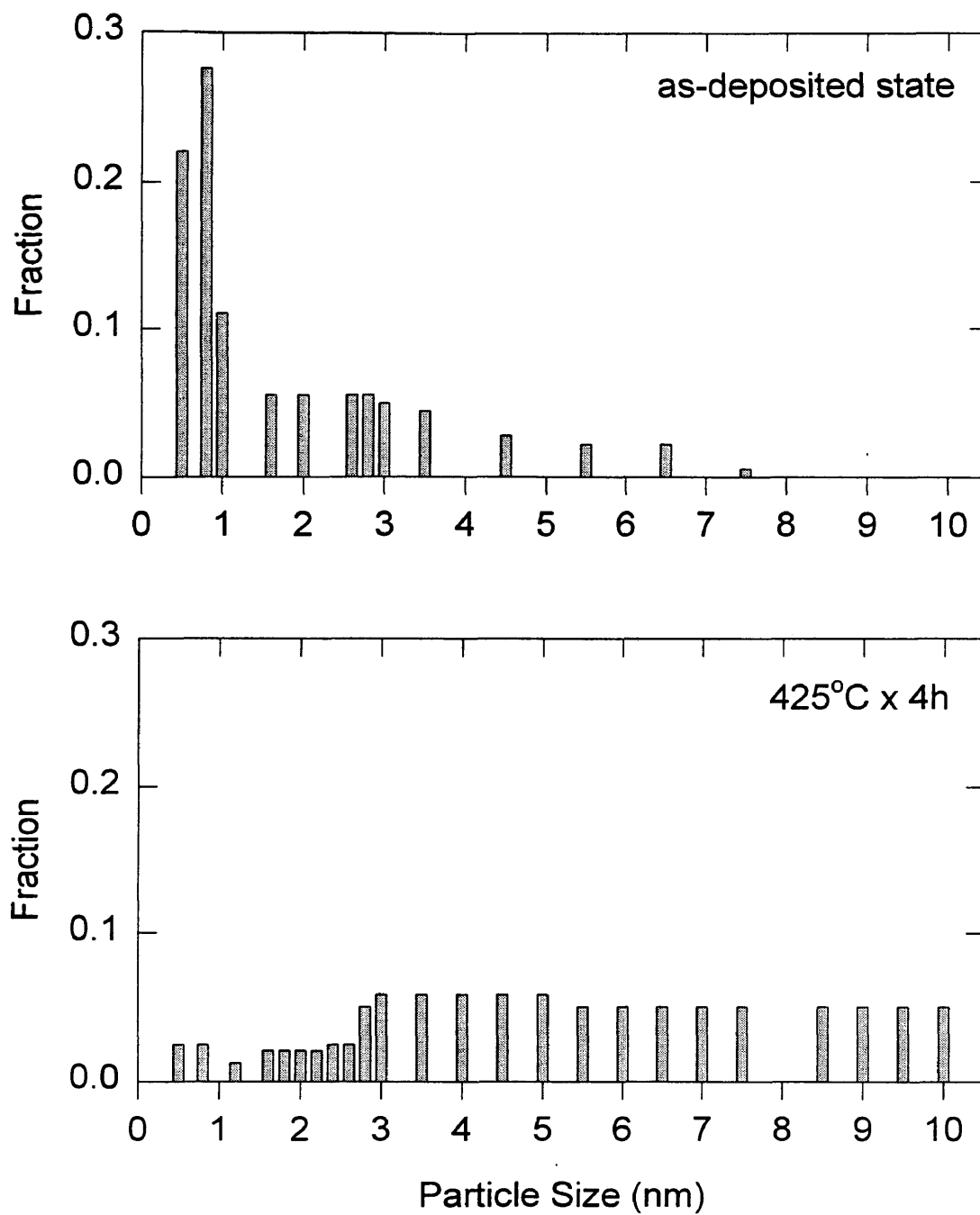


Fig. 26. The size distribution of nanovoids for the S1 sample

under the assumption of ellipsoidal nanovoids. This may be explained as Ostwald ripening or particle coarsening [43] in which the larger ones grow at the expense of the smaller ones. This is confirmed by the size distribution of nanovoids for S1, i.e., the nanovoids of below 1 nm radius are significantly decreased and larger ones above 6 nm are increased after the last annealing step as shown in Figure 26.

The systematic decrease in the intensity at large q ($4.1 \leq q \leq 6.2$) is due to the loss of H within the matrix, such that H evolution occurs with the increasing temperature. This decrease of diffuse scattering intensity is indicated in Figure 14 with the circle symbols.

5.3.2 High H content effects

Figure 10 shows the SAXS intensity from the H1 and H2 samples in the as-deposited state and upon annealing for 1 hour. Significant changes are caused by the annealing, and there is a clear increase of integrated SAXS intensity between 250°C and 300°C as shown in Figure 13. Annealing above 300°C causes systematic increases, and the volume fraction (V_f) and number density (N) of the low-density particles are both increased as shown in Figures 24 and 25.

The interference effect appears as a shoulder in the SAXS intensity weakly from 300°C and strongly from 350°C annealing. This effect is caused by a high density of scattering centers of similar size [21]. This shoulder is shifted to smaller q with

increasing temperature, and the average radius of nanovoids is also increased somewhat as shown in Table 4 and Figure 15.

Table 4. Results of SAXS analyses of the H1 sample, where T is the annealing temperature for 1 hour and D is the effective hard-sphere interaction diameter [30]. The value of D represents the size of the H diffusion zone around H_2 bubbles, such that D is significantly larger than $\langle 2R \rangle$.

T (°C)	Q (10^{24} eu/cm ³)	V_{f1} (%)	N (%)	$\langle R \rangle$ (nm)	D (nm)
300	2.4	0.33	0.26	0.46	1.7
350	6.3	0.91	0.7	0.51	1.85
375	7.2	1.08	0.46	0.69	2.4
400	7.5	1.05	0.35	0.78	2.7

For the H1 sample, the average ellipsoidal dimensions are increased from 0.9 x 1.3 nm at 300°C to 1.6 x 1.8 nm at 400°C. Furthermore, the nanovoids tend toward more spherical geometry with increasing temperature and a more prominent interference effect. The testing for anisotropy in the SAXS is shown in Figure 20. The nucleation of H_2 bubbles occurred up to 300°C with no increase of $\langle R \rangle$, then the growth of H_2 bubbles follows from 350°C leading to increasing $\langle R \rangle$ and the decreasing number density. This

result is confirmed from Figure 27 indicating the size distribution of nanovoids for the H1 sample.

The systematic decrease of diffuse scattering intensity is indicated with the triangle symbols in Figure 14, and it is compared with the S samples. For the H1 and H2 samples, they start with much stronger intensities and drop significantly in the 300°C annealing steps. This coincidence of the decreasing I_D and the appearance of interference behavior at the same time indicates that the H evolution in the H1 and H2 samples is directly related to the origin of nanovoids, or in other words, to the precipitation of H₂ bubbles.

5.4 Influence of germanium

Figure 13 shows that high Ge samples, H1 and H2, start to experience noticeable increases of Q between 250°C and 300°C. The diffuse scattering intensity of the H samples is also dropping significantly at the 300°C annealing stage as indicated in Figure 14. For $a-Si:H$ with high H content (~20 at. %), Q increases significantly from annealing above 350°C [17] which is higher than the 250°C - 300°C observed for $a-SiGe:H$ of H content (~20 at. %). This reduced microstructural stability may be due to the weaker Ge-H bonds [46] allowing more active H evolution from the $a-SiGe$ network. This result coincides with the earlier study by Nakashita et. al. [44], i.e., the Ge-H evolution occurs at relatively lower temperature than Si-H bonds.

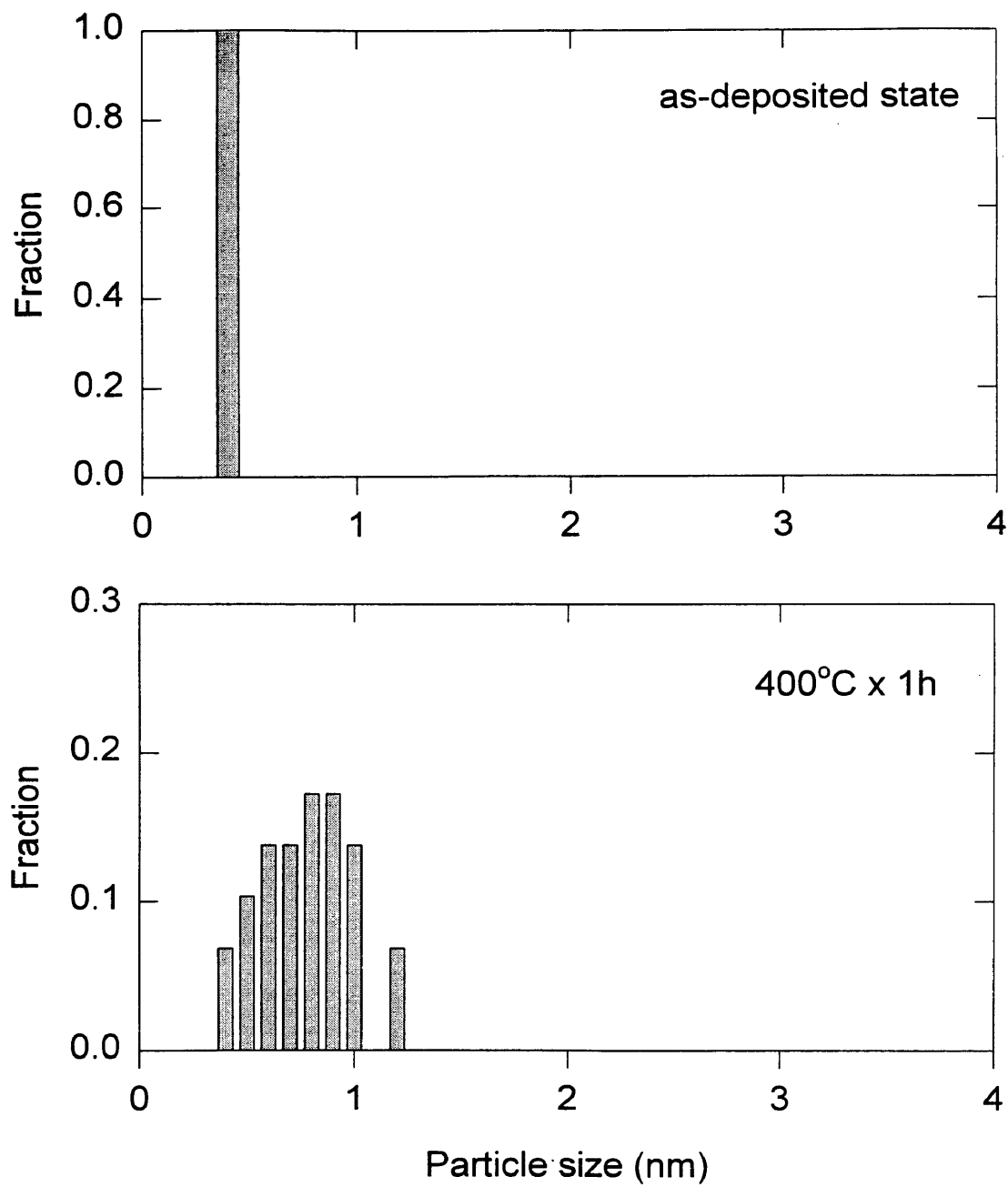


Fig. 27. The size distribution of nanovoids for the H1 sample

However, it is difficult to separate the relative importance of H and Ge on the microstructural stability since H1 and H2 have both high H and high Ge contents at the same time in this study. If samples which have the same Ge content but different H content, or the same H content but different Ge content are prepared, this might allow the influence of H and Ge contents to be more clearly distinguished.

5.5 H stability and solubility

An important parameter to observe the H stability and solubility is the diffuse scattering intensity, I_D as discussed in chapter 2. As shown in Figure 14, I_D drops more significantly for the H samples of high hydrogen content than the U and S samples of low hydrogen. This result coincides with the earlier study by Beyer [45], i.e., high H decreases the H stability upon annealing. Comparing with the I_D behavior for $a-Si:H$ [17] of similar H content with the present samples, $a-SiGe:H$ experiences more significant decrease (about 50 % versus 10 %), although there is some difference of annealing history up to 400°C in the two studies. This coincides with the result that the weaker Ge-H bonds yield the lower H stability suggested in section 5.4.

For the S samples, nanovoids induced from the H evolution are growing upon annealing, and the nanovoids for the H1 and H2 samples are increasing in number up to 300°C followed by growth from $\geq 350^\circ\text{C}$. This nucleation and growth is the clear indication for the existence of H above the solubility limit. The excess H above the

solubility limit probably does not play a role in the passivation of dangling bonds in amorphous matrix, and it forms an unstable structure building the local strain. However, during annealing, this strain associated with the excess H can be released by the precipitation in the form of H₂ bubbles.

To estimate the H solubility, I_D is used for the residual H quantity under the assumptions that H evolves with the same ratio of I_D decrease and H complexes causing the increase of I_D is negligible. For H1 sample, I_D decreases from 102 eu to 47 eu after annealing up to 400°C for 4 hours. Therefore, the residual H content is estimated at 6.5 - 8 at. % for the H1 and H2 samples. The S1 and S2 samples have 4.5 - 5.5 at. % H after annealing up to 425°C for 4 hours. Both of the residual H contents are higher than the 3 - 4 at. % H solubility limit found for annealing up to 550°C in *a-Si:H* [17]. However, the latter sample was prepared by implantation techniques and this is likely to lead to different H solubility. The H1 and H2 samples have higher H solubility than the S1 and S2 samples, and it may be due to the higher initial H content in the H1 and H2 samples.

5.6 Influence of initial microstructure

H2 and S2 samples have similar columnar-like initial microstructural features, although the H2 sample has smaller size than the S2 sample. The behavior of nanovoids for these samples are different, i.e., H2 experiences the nucleation of nano-bubbles and

S2 shows the growth of the nanovoids continuously. Therefore, the initial microstructure does not have a relation with microstructural stability and H solubility.

The most important impact of initial structure is to control the geometry of scattering particles, i.e., nanovoids, during growth. For S1 and S2 samples, the growing process proceeds with no nucleation of H₂ nano-bubbles as shown from the results of increasing V_f and decreasing N (Figures 24 and 25). Therefore, the nanovoids are growing more parallel to the elongated axis of ellipsoidal geometry upon annealing following the initially elongated features. This is confirmed by the larger $(Q_o / Q_{45})_N$ values observed, such that much more elongated ellipsoids are formed after the annealing step compared to the as-deposited state.

For H1 and H2 samples, the nucleation process proceeds before growing of nanovoids. The elongated initial structure is considerably changed toward spherical shape during nucleation process when the nanovoids are about to aggregate as indicated in Figure 23. Therefore, the nanovoids are aggregating with no preferential direction when H1 and H2 samples are growing above 350°C. Finally the more spherical nanovoids of larger size than the initial size are observed for the last annealing step (See Figures 15, 23, 24 and 25).

5.7 Tilting-effect

The tilting parameter $(Q_o / Q_{45})_N$ is changed differently depending on H contents and initial microstructure as mentioned in section 5.6. For samples S1 and S2, Figure 23 shows increased difference of $(Q_o / Q_{45})_N$ curves with increasing temperature, such that Q_o leads to exaggerated quantities of nanovoids along the direction of long axis. The reduced Q_{45} compared with Q_o is the clear indication of elongated features oriented with the long axis perpendicular to the film plane. Based on these $(Q_o / Q_{45})_N$ values, the Q values are corrected to an average, $\langle Q \rangle$, by the average over the angular range from 0 to $\frac{\pi}{2}$ as indicated in Figure 28 [29]. The S1 and S2 samples of highly elongated nanovoids show reduced $\langle Q \rangle$ after correction as compared with the measured Q curves in Figure 13.

Samples H1 and H2 have similar SAXS intensities between 0° and 45° tilting after 400°C x 4h annealing step (Figure 20). Because of almost spherical nanovoids, the measured Q values with no tilt are not much different from the averaged $\langle Q \rangle$ from 0 to $\frac{\pi}{2}$. Therefore, more significant $\langle Q \rangle$ of H1 and H2 are observed as compared with S1 and S2 samples with increasing temperature in Figure 28 (Compare with Figure 13).

Figure 28 shows that the U1 sample experienced almost no change of $\langle Q \rangle$ curves due to a small quantity of nanovoids, and the U2 sample decreases $\langle Q \rangle$

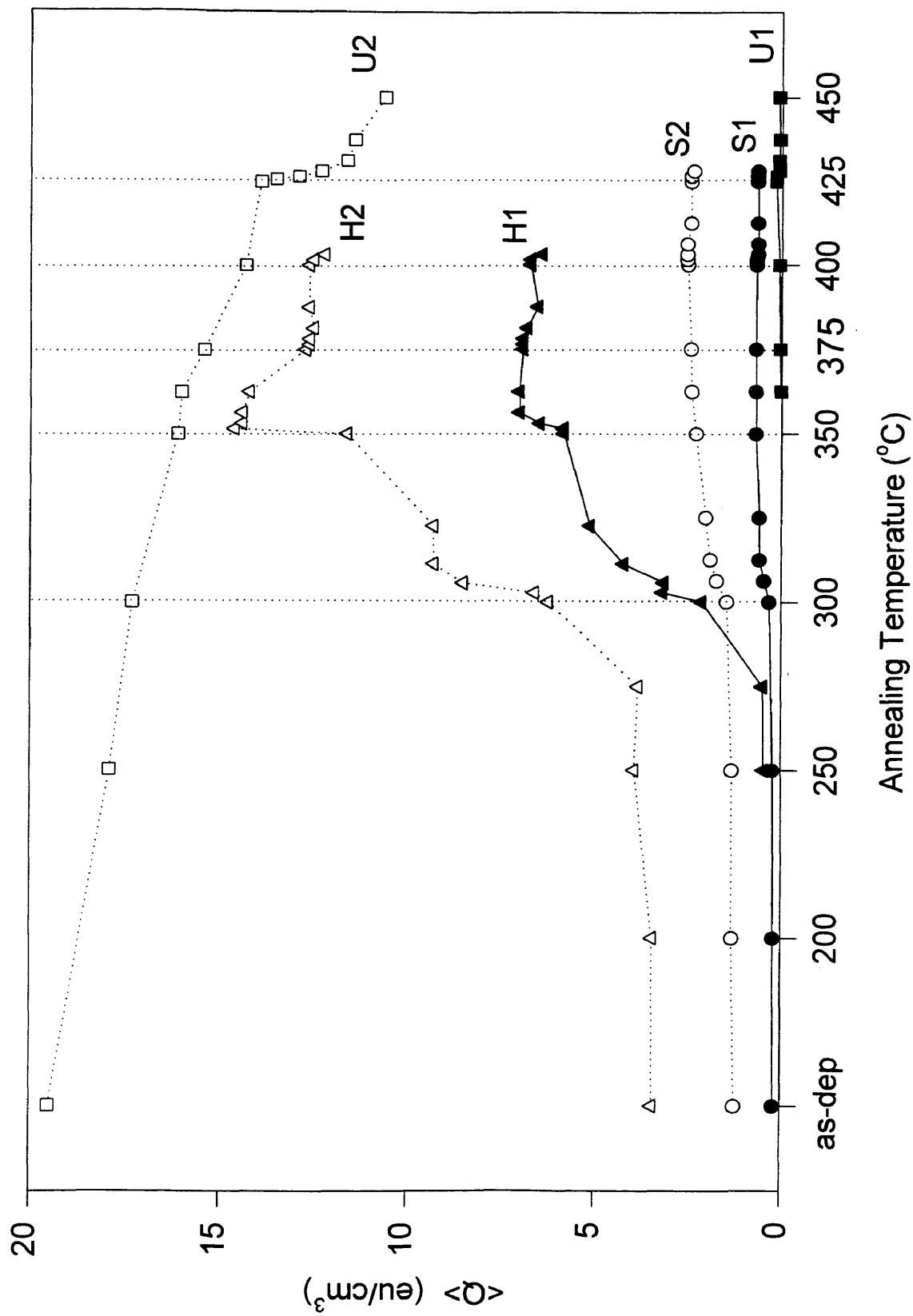


Fig. 28. $\langle Q \rangle$ corrected by angular range from 0 to $\frac{\pi}{2}$

continuously, similar to the Q behavior. Generally, the high H samples have more significant increases of the quantities of nanovoids than the case of the low H samples, even if they start at similar Q values in the as-deposited states as seen, e.g., with the H1 and S1 samples.

5.8 Time dependence

The annealing time behavior of the SAXS results has been studied at various annealing temperatures as indicated in Figure 13. The S, U and H samples appear to experience a diffusion-like process as seen in the time behavior of the average radius of nanovoids (Figure 15).

Figures 29-(a) and (b) show a measure of the average particle volume change, $\langle R(t) \rangle^3 - \langle R_o \rangle^3$, versus anneal time, t , for S1 and H1 samples, on a double-logarithmic scale where $\langle R_o \rangle$ is the average particle radius at $t = 0$. This plot is based on:

$$\langle R(t) \rangle^3 - \langle R_o \rangle^3 = ct^s, \quad (18)$$

where c is a constant depending on the annealing temperature, diffusion coefficient (D), and interface energy between the particles and amorphous matrix, and s is the time exponent to indicate the $\langle R \rangle$ dependence on the annealing time, t . The above rate Eq. (18) was used in an earlier study by Mantl [43] for CoSi_2 precipitates in Si, in which

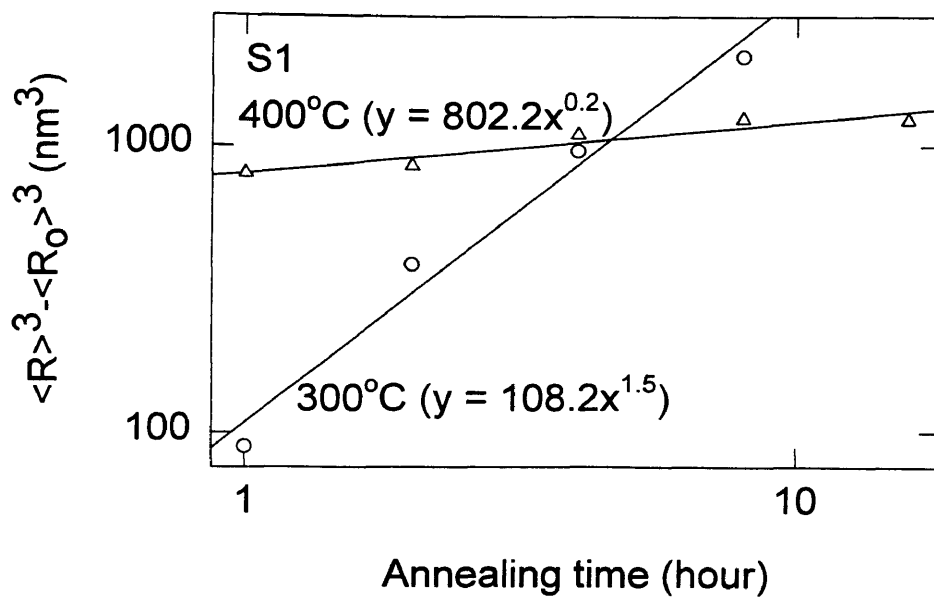
$\langle R(t) \rangle^3 - \langle R_0 \rangle^3$ increased linearly as a function of the annealing time, t , i.e., $s = 1$ and $\langle R_0 \rangle = 0$ based on the work by Lifshitz and Slyozov [47] and by Wagner [48] (LSW theory). In this model, coarsening occurs at almost a constant volume fraction with a reduction of the number density of the precipitates.

For the S1 sample, a power-law relationship of ellipsoidal volume change (by the product of the square of short axis and long axis) is observed with the annealing time with $s = 1.5$ for the 300°C series. However, 400°C annealing shows a power-law relationship with $s = 0.2$ which is much smaller than the exponent s for the 300°C. The larger s value for the 300°C than that of the 400°C coincides with the significant increase of $\langle R \rangle$ in Fig. 15.

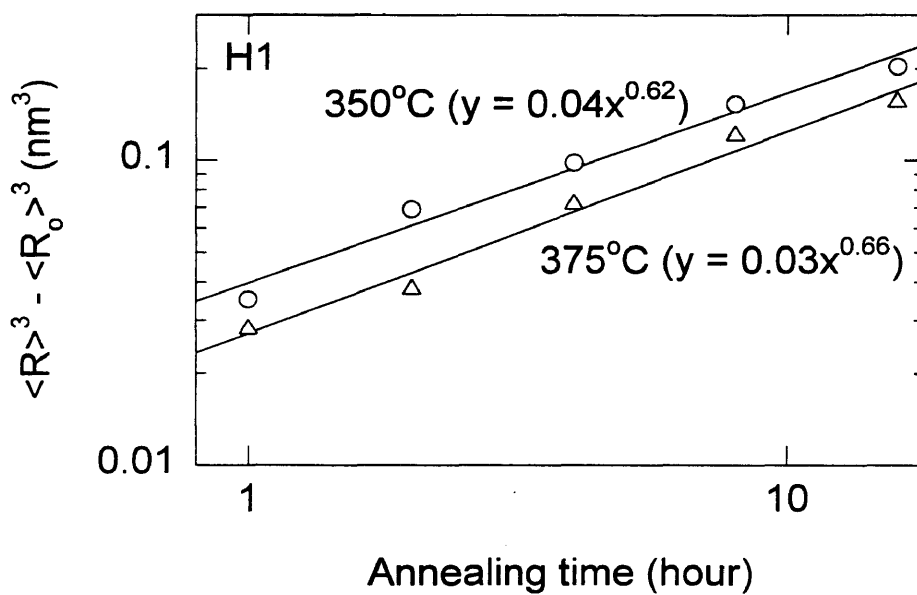
A power-law relationship of the volume change of nanovoids is observed for the H1 sample (Fig. 29-(b)) with $s = 0.62$ for 350°C and $s = 0.66$ for 375°C, in which the spherical-like nanovoids do not change much their shape upon annealing as shown in Figure 23. The smaller s values than the unity means that the coarsening rate is stabilized as time extends at the same temperature.

The different results from the former works by Mantl [43] and by Mergia et. al. [49], based on the $\langle R_0 \rangle = 0$ and the constant V_f of the precipitates, is probably due to the $\langle R_0 \rangle \neq 0$ and the changing V_f during the present experiments, as well as the changing geometry of the precipitates. Therefore, the volume of nanovoids does not increase by the ideal linear relationship as the annealing time increases.

Summarizing, the growing mechanism of nanovoids is following a diffusion-like process. The growth rate is decreased as annealing time increases, such that this growing mechanism is more dependent upon the annealing temperature than the annealing time.



(a)



(b)

Fig. 29. Time dependence of the average volume change of particles for (a) S1 and for (b) H1 samples.

Chapter 6

CONCLUSIONS

SAXS studies of the microstructural stability and hydrogen solubility of $a - Si_{1-x}Ge_x:H$ have been completed with several samples of selected Ge and H contents, different initial microstructures, and deposited at different substrate temperatures. Although it has been demonstrated earlier [9, 41] that the systematic increase in Ge content leads to increasing inhomogeneity in the nanostructure, within the set of samples examined here with wide variations in Ge content, as well as H content, nearly homogeneous nanostructure can be achieved by adjusting the deposition conditions. Upon heat treatment the microstructure experiences significant change depending on the following important features:

- i) In low H samples, S1 and S2, conglomeration or growth at the expense of small nanovoids occurs with increasing volume fraction and decreasing number density. Especially these voids are aggregating parallel to the deposition direction, such that elongated ellipsoidal nanovoids emerge from increasing annealing temperature. The growing geometry seems to depend upon the initially elongated microstructure.

- ii) For high H samples, H1 and H2, the nucleation of spherical H_2 bubbles promotes an increasing volume fraction of inhomogeneities with increasing annealing temperature. The slightly elongated nanovoids in the as-deposited state are probably dominated by the new spherical H_2 bubbles, and an interference effect due to a high density of inhomogeneities appears at $\geq 300^\circ\text{C}$ annealing stages. The H_2 bubbles start to grow spherically at the expense of smaller ones from 350°C because the initially elongated nanovoids are already changed to spherical-like shape during the nucleation process.
- iii) The weaker Ge-H bond, relative to the Si-H bond, leads to reduced microstructural stability based on the fact that the high Ge samples, H1 and H2, are observed to start significant changes in Q between 250°C and 300°C , and above 300°C for low Ge samples, S1 and S2, and above 350°C for $a - Si:H$ (i.e., no Ge) [17]. The residual H content is estimated at 6.5 - 8 at. % for the H1 and H2 samples after annealing up to 400°C for 4 hours and 4.5 - 5.5 at. % for the S1 and S2 samples after annealing up to 425°C for 4 hours, both of which are higher than the 3 - 4 at. % H solubility found for annealing up to 550°C in $a - Si:H$ [17]. The H solubility for $a - Si_{1-x}Ge_x:H$ has different values depending on the Ge content. The H1 and H2 samples have higher H solubility than the S1 and S2 samples, even though the H1 and H2 samples have smaller H stability. It seems to be due to the higher initial H content in the H1 and H2 samples.

- iv) The substrate temperature (T_s) during deposition does not directly control the geometry of nanovoids, but it implies that the microstructure below T_s can be quite stable. The high T_s sample, U1, shows little change of Q up to 450°C, while significant changes occur at $\geq 300^\circ\text{C}$ for the low T_s samples, S1, S2, H1 and H2. However U2 has a particularly interesting behavior, showing continuously *decreasing* Q up to 400°C followed by significantly larger changes versus time at 425°C. This is attributed to a metastable state created during the unbiased deposition, although the U2 sample is also deposited at the same temperature as the U1 sample. Decreasing volume fraction and number density indicates the disappearance of nanovoids with increasing temperature, which is confirmed from the increased flotation density compared with that of the as-deposited state. Based on the continuously decreasing diffuse scattering intensity (I_D), this disappearance of nanovoids may be due to a structural relaxation process aided by the active diffusion of H in the matrix.
- v) The coarsening mechanism of nanovoids is following a diffusion-like process. The growth rate decreases as annealing time increases, and it is more dependent upon the annealing temperature than the annealing time.
- vi) The H content in $a - Si_{1-x}Ge_x:H$ has an influence similar to the case of $a - Si:H$, i.e., high H induces lower H stability, leading to lower microstructural stability. However, the H solubility depends on both the initial H content and Ge

content. The weaker Ge-H bond affects the microstructural stability, but it is difficult to classify the effects of H or Ge contents exactly because both high H samples in this study have high Ge contents. These results are probably more dependent upon the H diffusion with temperature because H is the easiest element to diffuse in $a - Si_{1-x}Ge_x:H$.

Finally, some comments are in order on the relevance of these results to the fabrication of solar cells. The $a - SiGe:H$ alloys may be the first layer deposited at 200 - 400°C (See Fig. 1). During deposition of the $a - SiGe:H$ layer and during deposition of the rest of the layers, e.g., $a - Si:H$ and/or $a - SiC:H$, an annealing process takes place at the substrate temperature and can affect the alloy in ways demonstrated in this study, particularly if excess H above the solubility limit is included in the $a - SiGe:H$ layer. The internal defects developed during annealing can be detrimental to photoelectronic properties. However, as shown for the case of the U2 sample having poor initial microstructure, some improvement may occur during annealing that occurs during growth of the remaining cell layers.

REFERENCES

- [1] D. E. Carlson and C. R. Wronski, *Appl. Phys. Lett.* **28**, 671 (1976)
- [2] A. Catalano, R. Arya, B. Fiesemann, B. Goldstein, J. Newton, S. Wiedeman, M. Bennett and D. D. Carlson, *J. Non-Cryst. Solids.* **115**, 14, (1989)
- [3] K. Comoto, H Saitoh, A. Chida, H. Sannomiya, M. Itoh and Y. Yamamoto, *Solar Energy Materials and Solar Cells* **34**, 344 (1994)
- [4] S. Guha, S. Yang, J. Pawilkiewicz, A. Glatfelter, T. Ross and R. Ovshinsky, *Proceedings of the 20th Photovoltaic Specialists' Conference*, (New York, IEEE, 1988), p 79
- [5] D. L. Staebler and C. R. Wronski, *Appl. Phys. Lett.* **31**, 292 (1977)
- [6] K. D. Mackenzie and W. Paul, *J. Non-Cryst. Solids* **97 & 98**, 1055 (1987)
- [7] B. Von Roedern and A. Madan, *Philos. Mag. B* **63**, 293 (1991)
- [8] D. Jousse, E. Bustarret and F. Boulitrop, *Solid state Commun.* **55**, 435 (1985)
- [9] S. J. Jones, Y. Chen, D. L. Williamson, R. Zedlitz and G. Bauer, *Appl. Phys. Lett.* **62**, 3267 (1993)
- [10] S. J. Jones, Y. Chen, D. L. Williamson, X. Xu, J. Yang and S. Guha, *Mat. Res. Soc. Symp. Proc.* **297**, 815 (1993)
- [11] A. H. Mahan, P. Raboisson and R. Tsu, *Appl. Phys. Lett.* **50**, 335 (1987)
- [12] K. D. Mackenzie, J. R. Eggert, D. J. Leopold, Y. M. Li, S. Lin and W. Paul, *Phys. Rev. B* **31**, 2198 (1985)
- [13] I. Hirabayashi, K. Morigaki and S. Nitta, *Jpn. J. Appl. Phys.* **19**, 1357 (1980)

- [14] H. Dersch, J. Stuke and J. Beichler, *Appl. Phys. Lett.* **38**, 456 (1981)
- [15] P. Wickboldt, D. Pang, W. Paul, J. H. Chen, F. Zhong, J. D. Cohen, Y. Chen and D. L. Williamson, *J. Non-Cryst. Solids* **198-200**, 567 (1996)
- [16] S. Sugiyama, X. Xu, J. Yang and S. Guha, *Mat. Res. Soc. Symp. Proc.* **420**, 197 (1996)
- [17] S. Acco, D.L. Williamson, P.A. Stolk, F. W. Saris, M.J. van den Boogaard, W.C. Sinke, W.F. van der Weg, S. Roorda, and P.C. Zalm, *Phys. Rev. B.* **53**, 4415 (1996)
- [18] S. J. Jones, A. B. Swartzlander-Franz, Y. Chen and D. L. Williamson, *Mat. Res. Soc. Symp. Proc.* **297**, 1049 (1993)
- [19] K.M. Jones, D.L. Williamson, S. Acco and M.M. Al-Jassim, *Proceedings Microscopy and Microanalysis 1996*, Edited by G.W. Bailey (San Francisco Press, San Francisco 1996) p. 972
- [20] D. L. Williamson, *Mat. Res. Soc. Symp. Proc. Vol.* **377**, 254 (1995)
- [21] A. Guinier and G. Fournet, *Small-Angle Scattering of X-rays* (John Wiley and Sons, Inc., New York, 1955)
- [22] L.A. Feigin and D.I. Svergun, *Structure Analysis by Small-Angle X-ray and Neutron Scattering* (Plenum, New York, 1987)
- [23] G. Porod, in *Small-Angle X-ray Scattering*, Edited by O. Glatter and O. Krattky (Academic Press, New York, 1982)
- [24] P. Fratzl, S. Klaumuzer, M. Rammensee and G. Vogl, *Europhys. Lett.* **11**, 547 (1990)
- [25] G. C. Stutzin, R. M. Ostrom, A. Gallagher and D.M. Tanenbaum, *J. Appl. Phys.* **74**, 1 (1993)
- [26] Y. J. Chabal and C. K. N. Patel, *Rev. Mod. Phys.* **59**, 835(1987)
- [27] E. Bustarret, E. Sauvain and M. Ligeon, *Phil. Mag. Lett.* **75**, 35(1997)

- [28] D. W. Schaefer, R. K. Brow, B. J. Oliver, T. Rieker and G. Beaucage, in *Modern Aspects of Small-Angle Scattering*, Edited by H. Brumberger (Kluwer Academic Publisher, Dordrecht, 1995) p. 299
- [29] M. Shibayama, S. Nomura, T. Hashimoto, and E. L. Thomas, *J. Appl. Phys.* **66**, 4188 (1989)
- [30] N. W. Ashcroft and J. Lekner, *Phys. Rev.* **145**, 83 (1966)
- [31] L. H. Schwartz and J. B. Cohen, *Diffraction from Materials* (Springer, Berlin, 1987) p. 155
- [32] *International Tables for X-ray Crystallography*, Vol. 3 (Kynoch Press, New York, 1986) p. 247
- [33] A. Guiner, *X-ray Diffraction* (W. H. Freeman and Company, 1963) p. 193
- [34] *International Tables for X-ray Crystallography*, Vol. 3 (Kynoch Press, New York, 1986) p. 232
- [35] A. M. Levelut and A. Guinier, in *Small-Angle X-ray Scattering*, Edited by H. Brumberger (Gordon and Breach, New York, 1967) p. 351
- [36] B. E. Warren, *X-ray Diffraction* (Dover, New York, 1969) p. 227
- [37] W. S. Rothwell, *J. Appl. Phys.* **41**, 4459 (1970)
- [38] Y. Chen, *Microstructure Study of Amorphous silicon-based Semiconductors by Small Angle X-ray Scattering*, Ph.D. Thesis (T-4492), Colorado School of Mines, 1994
- [39] D. L. Williamson, A. H. Mahan, B. P. Nelson, and R. S. Crandall, *Appl. Phys. Lett.* **55**, 783 (1989)
- [40] *Alloy Diffuse Scattering Studied by Small Angle X-ray Scattering*, D. Min, MS Thesis (T-4798), Colorado School of Mines, 1995
- [41] A. R. Middya, S. Ray, S. J. Jones and D. L. Williamson, *J. Appl. Phys.* **78**, 4966 (1995)

- [42] J. T. Koberstein, B. Morra and R. S. Stein, *J. Appl. Cryst.* **13**, 34 (1980)
- [43] S. Mantl, *Mat. Sci. Rep.* **8**, 1 (1992)
- [44] T. Nakashita, A. Inoue, S. Hagiwara, F. Uehara and K. Kohno, *Jpn. J. Appl. Phys.* **31**, 1730 (1992)
- [45] W. Beyer, 16th International Conference on Amorphous Semiconductors, Kobe, Japan, 4.-8 September 1995
- [46] Stanford R. Ovshinsky, *Solar Energy Mat. and Solar Cells* **32**, 443 (1994)
- [47] I. M. Lifshitz and U. V. Slyozov, *J. Phys. Chem. Solids* **19**, 35 (1961)
- [48] C. Wagner, *Z. Elektrochem.* **65**, 35 (1961)
- [49] K. Mergia, F. Al-Hazmi, R. J. Stewart and S. Messoloras, *Phil. Mag. A* **75**, 939 (1997)